ISSN: 2754-4753

Journal of Physics & Optics Sciences

SCIENTIFIC Research and Community

Review Article

Open Access

Relativistic Vlasov-Maxwell Simulations of the Seed Pulse Amplification in Plasmas by Stimulated Raman and Brillouin Backscattering

Magdi Shoucri

Retired Senior Senior Scientist, Hydro-Québec Research Institute (IREQ), Varennes, Quebec, Canada J3X1S1

ABSTRACT

We apply a Eulerian Vlasov code for the numerical solution of the relativistic Vlasov-Maxwell equations to study the problem of the amplification of an ultra-short seed pulse via stimulated Raman or Brillouin backscattering from a long pump pulse, assumed to have an envelope with a constant amplitude, in plasmas. An analysis of the spectra of waves which participate in the amplification processes is presented, calculated by the numerical code, showing good agreement with the available predicted theoretical values. The evolution showing the pump depletion, accompanied by the counter-propagating seed-pulse amplification, compression and increased steepness of the waveform is also presented, and accurate contour plots of the distribution functions. In recent numerical simulations, it has also been shown that besides the stimulated Raman backscattering SRBS and the stimulated Brillouin backscattering SBBS, other high and low frequency kinetic instabilities can occur when evolving modes develop in the modified distribution functions during the evolution of the system. We study the wave effects of these kinetic instabilities on the stimulated Raman scattering and stimulated Brillouin scattering short pulses amplification processes. The absence of spurious noise in grid based Eulerian Vlasov codes allows to follow the evolution of the system with a fully kinetic description and accurate representation of the phase-space structures coexisting and interacting in the electron distribution function. We present results which compare favourably with what can be obtained from particle-in-cell (PIC) codes.

***Corresponding author**

Magdi Shoucri, Retired Senior Senior Scientist, Hydro-Québec Research Institute (IREQ), Varennes, Quebec, Canada J3X1S1.

Email: magshoucri@gmail.com

Received: March 02, 2026; **Accepted:** March 13, 2026; **Published:** March 23, 2026

Keywords: Seed Pulse, Eulerian Codes, Relativistic Vlasov-Maxwell

1. Introduction

In the last few decades there have been important developments and applications of Eulerian codes for the numerical solutions of the kinetic equations of plasmas. The methods which discretize the full phase-space on a multi-dimensional grid and perform the direct solution of the distribution function on this grid, by solving numerically the partial differential equations for the distribution functions in the multi-dimensional phase-space, are called Eulerian methods. Of special interest are the Eulerian codes based on the method of characteristics for hyperbolic differential equations, because of the absence of numerical noise they allow an accurate study of the phase-space dynamics, especially in the low-density regions of the phase-space. This approach has become increasingly important, especially for the numerical solution of the hyperbolic type Vlasov-Maxwell equations, which are used to study the kinetic processes when the collisions between the particles are negligible, as in high temperature and low-density plasmas. The areas of the kinetic processes in plasmas are broad, and of special interest are the applications to the study of collision less transport processes using the Vlasov equation for a wide range of phenomena displaying collective behaviour [1-6].

In the present work, we present applications of Eulerian codes for the numerical simulation of seed pulses amplification in plasmas. Special attention has been given recently to the idea of plasma-based laser amplifiers for their application to the direct amplifications of ultra-short laser pulses through the stimulated Raman backscattering SRBS or the stimulated Brillouin backscattering SBBS. For the application to the problem of plasma-based laser amplifiers, which is the direct amplification of ultra-short laser pulses, the stimulated Raman backscattering SRBS is the interaction of the pump light wave with a daughter light seed wave propagating in the opposite direction, where the transfer of energy is mediated via a high frequency electron plasma wave EPW response. And the stimulated Brillouin backscattering SBBS is the interaction of a pump light wave with a daughter light seed wave propagating in the opposite direction, where the transfer of energy is mediated via an ion plasma wave, usually the plasma response in this case is a low frequency ion acoustic wave IAW. These processes involve the collision of the long pump pulse with the ultra-short seed pulse propagating in the opposite direction, in order to amplify the seed pulse intensity by several orders of magnitude. The seed pulse convectively grows with interaction distance as does the plasma mode (EPW or IAW). But as the seed pulse grows, it also depletes the pump energy. Promising experimental and numerical simulations results have been predicted or reported. We mention as examples, recent and less recent, the works of Drake et al., Malkin et al., Max et al., Kruer, Mourou et al., Riconda et al., Benisti et al., Lehmann et al., Wang et al., Toroker et al., Shoucri et al., Califano et al., [7-22].

In these new developments transient propagation effects become important. Numerical simulations have shown that besides stimulated Raman backward scattering SRBS and forward scattering SRFS, or stimulated Brillouin backward scattering

SBBS and forward scattering SBFS, other high frequency kinetic instabilities can occur when modified distribution functions exist during the transient evolution of the system. We identify them by the name kinetic electrostatic electron nonlinear (Keen) waves [18,20]. There have also been associations of beam acoustic modes BAM with SRBS nonlinear evolution and saturation. Electron acoustic waves EAW association have also been suggested. A different perspective has also been promulgated under the heading of transient enhanced instability levels attributed to rapidly changing distribution functions which diminish damping rates and thus allow larger levels of SRS than would be expected in models ignoring transient tracking of distribution functions. Of these Keen waves have the interesting features that they are not steady state, time-independent solutions, but rather transient evolving solutions. More discussions on the kinetic electrostatic electron nonlinear Keen waves can be found in Shoucri et al., [18,20].

There is great advantage to apply the Eulerian codes to study these problems because of the absence of numerical noise in these codes, they offer the possibility to distinguish clearly the excited modes, especially those excited during the evolving transient phases of the distribution function. In contrast, the noisy particle-in-cell (PIC) codes with other associated numerical problems like excessive pump scattering and depletion from the numerical noise, make it difficult to get a fine resolution. The absence of noise in the Eulerian Vlasov codes allows accurate representation of the phase-space structures of the distribution function, and accurate identification of the modes involved in the physics of the scattering processes, especially when relevant to the transient evolution of the system. Eulerian Vlasov codes have successfully been applied to the numerical solution of the relativistic Vlasov-Maxwell equations to study in a plasma the amplification of ultra-short seed pulses via stimulated Raman or Brillouin backscattering, from a long plasma pulse, assumed of constant amplitude before interaction [18-21].

In the present work we apply an Eulerian Vlasov code for the numerical solution of relativistic one-dimensional Vlasov-Maxwell equations to study two problems of seed pulse amplification. The problem of the amplification of an ultra-short seed pulse by SRBS when the plasma response is mediated by a plasma wave, and the problem of the amplification of an ultra-short seed pulse by SBBS when the plasma response is mediated by an ion acoustic wave IAW [18-20]. In both cases the long pump pulse is assumed to have an envelope that is constant in amplitude before interaction. But as the seed pulse grows, it also depletes the pump energy. Detailed analysis of the spectra developed during the amplification process will be presented, together with the evolution showing the pump depletion, accompanied by the counter-propagating seed-pulse amplification, compression and increased steepness of the waveform. Also detailed contour plots of the distribution functions will be presented,

2.The Relevant Equations and the Numerical Scheme of the Relativistic Vlasov-Maxwell Equations

Time t is normalized to the inverse electron plasma frequency ω_{pe}^{-1}, length is normalized to $l_0 = c\omega_{pe}^{-1}$, velocity and momentum are normalized respectively to the velocity of light c and to $m_e c$. The general form of the Vlasov equation is written for the present problem in a 4D phase-space for the electron distribution function $F_i(x, p_{xi}, p_{yi}, p_{zi}, t)$ and the ion distribution function $F_i(x, p_{xi}, p_{yi}, p_{zi}, t)$ (one spatial dimension) as follows (Shoucri 2008a,b, Shoucri et al., 2003, 2004. 2014, 2015, 2016a):

$$\frac{\partial F_{e,i}}{\partial t} + \frac{p_{xe,i}}{M_{e,i}\gamma_{e,i}}\frac{\partial F_{e,i}}{\partial x} \mp (\vec{E} + \frac{\vec{p}_{e,i} \text{ x } \vec{B}}{\gamma_{e,i}}) \cdot \frac{\partial F_{e,i}}{\partial \vec{p}_{e,i}} = 0 \quad (1)$$

with

$$\gamma_{e,i} = \left(1 + \frac{1}{M_{e,i}^2}(p_{xe,i}^2 + p_{ye,i}^2 + p_{ze,i}^2)\right)^{1/2} \quad (2)$$

(the upper sign in Eq. (1) is for electrons and the lower sign for ions, and subscripts *e* or *i* denote electrons or ions respectively). In our normalized units $M_e = 1$ and $M_i = \frac{m_i}{m_e}$.

We write the Hamiltonian of a particle in the electromagnetic field of the wave:

$$H_{e,i} = M_{e,i}(\gamma_{e,i} - 1) \mp \varphi(x,t). \quad (3)$$

where φ (x,t) is the scalar potential. Eq.(1) can be reduced to a two-dimensional phase-space Vlasov equation as follows. The canonical momentum $\vec{P}_{ce,i}$ is connected to the particle momentum $\vec{p}_{e,i}$ by the relation $\vec{P}_{ce,i} = \vec{p}_{e,i} \mp \vec{a}$. $\vec{a} = e\vec{A}/m_e c$ is the normalized vector potential. From Eq. (3), we can write:

$$H_{e,i} = M_{e,i}\left(\left(1 + \frac{1}{M_{e,i}^2}(\vec{P}_{ce,i} \pm \vec{a})^2\right)^{1/2} - 1\right) \mp \varphi(x,t). \quad (4)$$

Choosing the Coulomb gauge ($div\vec{a} = 0$), we have for our one-dimensional problem $\frac{\partial a_x}{\partial x} = 0$, hence $a_x = 0$. The vector potential $\vec{a} = \vec{a}_\perp(x,t)$, and we also have the following relation along the longitudinal direction:

$$\frac{dP_{cxe,i}}{dt} = -\frac{\partial H_{e,i}}{\partial x} \quad (5)$$

and since there is no transverse dependence

$$\frac{d\vec{P}_{c\perp e,i}}{dt} = -\nabla_\perp H_{e,i} = 0. \quad (6)$$

This last equation means $\vec{P}_{c\perp e,i}$ = const. We can choose this constant to be zero without loss of generality, which means that initially all particles at a given (x,t) have the same perpendicular momentum $\vec{p}_{\perp e,i} = \pm\vec{a}_\perp(x,t)$. The Hamiltonian now is written:

$$H_{e,i} = M_{e,i}\left(\left(1 + p_{xe,i}^2/M_{e,i}^2 + a_\perp^2(x,t)/M_{e,i}^2\right)^{1/2} - 1\right) \mp \varphi(x,t) \quad (7)$$

The 4D distribution function $F_{e,i}(x, p_{xe,i}, \vec{p}_{\perp e,i}, t)$ can now be reduced to a 2D distribution function

$f_{e,i}(x, p_{xe,i}, t)$:

$$F_{e,i}(x, p_{xe,i}, \vec{p}_{\perp e,i}, t) = f_{e,i}(x, p_{xe,i}, t)\delta(\vec{p}_{\perp e,i} \mp \vec{a}_\perp). \quad (8)$$

$f_{e,i}(x, p_{xe,i}, t)$ verify the relation:

$$\frac{df_{e,i}}{dt} = \frac{\partial f_{e,i}}{\partial t} + \frac{\partial H_{e,i}}{\partial p_{xe,i}}\frac{\partial f_{e,i}}{\partial x} - \frac{\partial H_{e,i}}{\partial x}\frac{\partial f_{e,i}}{\partial p_{xe,i}} = 0 \quad (9)$$

which gives the following Vlasov equations for the electrons and the ions:

$$\frac{\partial f_{e,i}}{\partial t}+\frac{p_{xe,i}}{M_{e,i}\gamma_{e,i}}\frac{\partial f_{e,i}}{\partial x}+(\mp E_x-\frac{1}{2M_{e,i}\gamma_{e,i}}\frac{\partial a_\perp^2}{\partial x})\frac{\partial f_{e,i}}{\partial p_{xe,i}}=0\,. \quad (10)$$

where

$$\gamma_{e,i}=\left(1+\left(p_{xe,i}/M_{e,i}\right)^2+\left(a_\perp/M_{e,i}\right)^2\right)^{1/2}.$$

$$E_x=-\frac{\partial\varphi}{\partial x} \quad \text{and} \quad \vec{E}_\perp=-\frac{\partial\vec{a}_\perp}{\partial t} \quad (11)$$

and Poisson's equation is given by:

$$\frac{\partial^2\varphi}{\partial x^2}=\int f_e(x,p_{xe})dp_{xe}-\int f_i(x,p_{xi})dp_{xi} \quad (12)$$

An alternative way, used in the present work, is to calculate E_x from Ampère's equation: $\frac{\partial E_x}{\partial t}=-J_x$,

The transverse electromagnetic fields E_y, B_z and E_z, B_y for the circularly polarized wave obey Maxwell's equations. With $E^\pm=E_y\pm B_z$ and $F^\pm=E_z\pm B_y$, we write these equations in the following form:

$$(\frac{\partial}{\partial t}\pm\frac{\partial}{\partial x})E^\pm=-J_y\,.\;; \qquad (\frac{\partial}{\partial t}\mp\frac{\partial}{\partial x})F^\pm=-J_z \quad (13)$$

which are integrated along their vacuum characteristic $x=t$. In our normalized units we have the following expressions for the normal current densities:

$$\vec{J}_\perp=\vec{J}_{\perp e}+\vec{J}_{\perp i}\;; \qquad \vec{J}_{\perp e,i}=-\frac{\vec{a}_\perp}{M_{e,i}}\int_{-\infty}^{+\infty}\frac{f_{e,i}}{\gamma_{e,i}}dp_{xe,i}\,. \quad (14)$$

2A.The Numerical Scheme of the Eulerian Vlasov Code

We use a method of characteristics for the numerical solution of hyperbolic type partial differential equations. These methods are Eulerian methods which use a computational mesh to discretize the equations on a fixed grid, and have been successfully applied to different important problems in plasma physics [2,3,5,6,18-25].

The numerical scheme to advance Eq. (10) from time t_n to t_{n+1} necessitates the knowledge of the electromagnetic field $E^\pm$ and $F^\pm$ at time $t_{n+1/2}$. This is done using a centered scheme where we integrate Eq. (13) exactly along the vacuum characteristics with $\Delta x=\Delta t$, to calculate $E^{\pm n+1/2}$ and $F^{\pm n+1/2}$ as follows:

$$E^\pm(x\pm\Delta t,t_{n+1/2})=E^\pm(x,t_{n-1/2})-\Delta tJ_y(x\pm\Delta t/2,t_n) \quad (15)$$

with $J_y(x\pm\Delta t/2,t_n)=\frac{J_y(x\pm\Delta x,t_n)+J_y(x,t_n)}{2}$

A similar equation can be written for $F^{\pm n+1/2}$. From Eq. (11) we also have $\vec{a}_\perp^{n+1}=\vec{a}_\perp^{n}-\Delta t\vec{E}_\perp^{n+1/2}$, from which we calculate $\vec{a}_\perp^{n+1/2}=(\vec{a}_\perp^{n+1}+\vec{a}_\perp^{n})/2$. To calculate $E_x^{n+1/2}$, two methods can be used.

A first method calculates E_x^n from $f_{e,i}^n$ using Poisson's equation, then we use a Taylor expansion

$$E_x^{n+1/2}=E_x^n+\frac{\Delta t}{2}\left(\frac{\partial E_x}{\partial t}\right)^n+0.5\left(\frac{\Delta t}{2}\right)^2\left(\frac{\partial^2E_x}{\partial t^2}\right)^n;$$
$$\text{with } \left(\frac{\partial E_x}{\partial t}\right)^n=-J_x^n; \qquad \left(\frac{\partial^2E_x}{\partial t^2}\right)^n=-\left(\frac{\partial J_x}{\partial t}\right)^n \quad (16)$$

$$J_x^n=\frac{1}{M_i}\int_{-\infty}^{+\infty}\frac{p_{xi}}{\gamma_i}f_i^n dp_{xi}-\frac{1}{M_e}\int_{-\infty}^{+\infty}\frac{p_{xe}}{\gamma_e}f_e^n dp_{xe}$$

A second method is to calculate $E_x^{n+1/2}$ from Ampère's equation: $\frac{\partial E_x}{\partial t}=-J_x$ from which $E_x^{n+1/2}=E_x^{n-1/2}-\Delta tJ_x^n$. See the discussion at Eq. (12) above.

Equation (10) is solved using the following scheme. Given $f_{e,i}^n$ at mesh points (we stress here that the subscript *i* denotes the ion distribution function), we calculate the new value $f_{e,i}^{n+1}$ at the grid points j_x, and j_p corresponding to the mesh points (x_{j_x},p_{xe,ij_p}) by writing that the distribution [2,3,5,6,18-20]:

$$f_{e,i}^{n+1}(x,p_{xe,i})=f_{e,i}^n(x-2\Delta_{xe,i},p_{xe,i}-2\Delta_{p_{xe,i}})\;; \quad (17)$$

$\Delta_{xe,i}$ and $\Delta_{p_{xe,i}}$ are calculated as follows from the solution of the characteristic's equations for Eq. (10), which are given by:

$$\frac{dx}{dt}=\frac{1}{M_{e,i}}\frac{p_{xe,i}}{\gamma_{e,i}}$$
$$\frac{dp_{xe,i}}{dt}=\mp E_x-\frac{1}{2M_{e,i}\gamma_{e,i}}\frac{\partial a_\perp^2}{\partial x}\,. \quad (18)$$

We use the following vectorial notation for Eq. (18):

$$.\;\mathbf{V}_{e,i}=\left(\frac{1}{M_{e,i}}\frac{p_{xe,i}}{\gamma_{e,i}},\mp E_x^{n+1/2}-\frac{1}{2M_{e,i}\gamma_{e,i}}\frac{\partial(a_\perp^{(n+1/2)})^2}{\partial x}\right) \quad (19)$$

We assume that at the time $t_{n+1}\equiv t_n+\Delta t$, x is at the grid point j_X, and $p_{xe,\,i}$ is at the grid point j_p. The following leapfrog scheme can be written for the solution of Eqs. (18):

$$\frac{x_{j_x}-x(t_n)}{\Delta t}=V_{xe,i}(x^{n+1/2},p_{xe,i}^{n+1/2})=V_{xe,i}(\frac{x_{j_x}+x(t_n)}{2},\frac{p_{xe,ij_p}+p_{xe,i}(t_n)}{2})\;. \quad (20)$$

$$\frac{p_{xe,ij_p}-p_{xe,i}(t_n)}{\Delta t}=V_{p_{xe,i}}(x^{n+1/2},p_{xe,i}^{n+1/2})=V_{p_{xe,i}}(\frac{x_{j_x}+x(t_n)}{2},\frac{p_{xe,ij_p}+p_{xe,i}(t_n)}{2}) \quad (21)$$

where $(x(t_n),p_{xe,i}(t_n))$ is the point where the characteristic is originating at t_n (not necessarily a grid point).

Put $\Delta_{xe,i} = \dfrac{x_{j_x} - x(t_n)}{2}$; $\Delta_{p_{xe,i}} = \dfrac{p_{xe,ij_p} - p_{xe,i}(t_n)}{2}$.

Equations (20) and (21) can be rewritten as:

$$\Delta_{xe,i} = \frac{\Delta t}{2} V_{xe,i}(x_{j_x} - \Delta_{xe,i}, p_{xe,ij_p} - \Delta_{p_{xe,i}}). \qquad (22)$$

$$\Delta_{p_{xe,i}} = \frac{\Delta t}{2} V_{p_{xe,i}}(x_{j_x} - \Delta_{xe,i}, p_{xe,ij_p} - \Delta_{p_{xe,i}}). \qquad (23)$$

Which are implicit equations for $\Delta_{xe,i}$ and $\Delta_{p_{xe,i}}$ and are solved by iteration. This iteration is done as follows. With Eq. (19) we rewrite Eqs. (22,23) in the vectorial form:

$$\Delta_{\mathbf{X}e,i} = \frac{\Delta t}{2} \mathbf{V}_{e,i}(\mathbf{X}_{e,i} - \Delta_{\mathbf{X}e,i}, t_{n+1/2}) \ . \qquad (24)$$

$\mathbf{X}_{e,i}$ is the two-dimensional vector $\mathbf{X}_{e,i} = (x, p_{xe,i})$, and $\Delta_{\mathbf{X}e,i} = (\Delta_{xe,i}, \Delta_{p_{xe,i}})$ is the two-dimensional vector calculated from the implicit relation in Eq, (22,23).

Eq. (24) for $\Delta_{\mathbf{X}e,i}$ is implicit and is solved iteratively:

$$\Delta^{k+1}_{\mathbf{X}e,i} = \frac{\Delta t}{2} \mathbf{V}_{e,i}(\mathbf{X}_{e,i} - \Delta^{k}_{\mathbf{X}e,i}, t_{n+1/2}),$$

where we start the iteration with $\Delta^{0}_{\mathbf{X}e,i} = 0$ for k=0. Usually, two or three iterations are sufficient to get a good convergence. We now write that the distribution function is constant along the characteristics. Then $f^{n+1}_{e,i}$ is calculated from $f^{n}_{e,i}$ in the relation written in Eq. (17), written here in the vectorial form:

$$f^{n+1}_{e,i}(\mathbf{X}_{e,i}) = f^{n}_{e,i}(\mathbf{X}_{e,i} - 2\Delta_{\mathbf{X}e,i}) \ ;$$

The shifted values are calculated by a two-dimensional interpolation using a tensor product of cubic *B*-splines [2,3,5,6,19,20].

The interpolation function is written in the form:

$$s(x, p_x) = \sum_{j=0}^{N_r} \sum_{k=0}^{N_\theta} \eta_{jk} B_j(x) B_k(p_x) \qquad (25)$$

For the calculation of the coefficients of the B-spline interpolation function $s(x,px)$, the coefficients η_{jk} are calculated from the values of the function at the grid points. The cubic B-spline is defined as follows:

$$B_j(x) = \frac{1}{6h^3} \begin{cases} (x - x_j)^3 & x_j \le x < x_{j+1} \\ h^3 + 3h^2(x - x_{j+1}) + 3h(x - x_{j+1})^2 & \\ \quad -3(x - x_{j+1})^3 & x_{j+1} \le x < x_{j+2} \\ h^3 + 3h^2(x_{j+3} - x) + 3h(x_{j+3} - x)^2 & \\ \quad -3(x_{j+3} - x)^3 & x_{j+2} \le x < x_{j+3} \\ (x_{j+4} - x)^3 & x_{j+3} \le x < x_{j+4} \end{cases} \qquad (26)$$

and $B_j(x) = 0$ otherwise. h is the grid size. A similar definition holds for $B_k(p_x)$. Details on the application of the algorithm are presented in [2,3,5,6,19,20].

3. Simulation of the Seed Pulse Amplification in Plasmas by Stimulated Raman Backscattering

We analyze the results of a simulation for the seed pulse amplification by stimulated Raman backscattering in an underdense plasma, using parameters similar to those presented in Mourou et al., [11]. A characteristic parameter by which to refer to the amplitude of laser field is the normalized vector potential or quiver momentum $|\vec{a}_\perp| = |e\vec{A}_\perp / M_e c| = a_0$ where $\vec{A}_\perp$ is the vector potential of the wave is $a_0^2 = I\lambda_0^2 /$ 1.368x1018. Here, I is the laser intensity in W/cm^2, and λ_0 the laser wavelength sn microns. The pump wave frequency ω_{0P} of the injected laser beam is such that $\omega_{0P} / \omega_{pe} = 1/\sqrt{n/n_{cr}}$ where n_{Cr} is the critical density for the pump. In our calculation n/n_{cr} =0.099, which corresponds in this case to the pump wave frequency of the injected laser beam $\omega_{0P} = 1/\sqrt{n/n_{cr}}$ = 3.18 (normalized to the plasma frequency ω_{pe}), will be used in this normalized form in the remaining of thp text, n_{cr} is the critical density for the pump). In the present calculation the wavelength of the pump is λ_{0p} =1.05μm , and the laser intensity is $I_{0P} = 2\text{x}10^{15} W/cm^2$, which corresponds to an amplitude of the vector potential of the pump $a_{0P} = 0.04$.

The seed Raman backscattered pulse has a frequency $\omega_{0B} = 2.1657$ and a wavelength $\lambda_{0B} = 1.541\mu m$ .The laser intensity is $I_{0B} = 1\text{x}10^{14} W/cm^2$ which corresponds to an amplitude of the vector potential of the seed pulse $a_{0B} = 0.01318$

The frequency and wavenumber (ω_{0P}, k_{0P}) of the pump wave are related in normalized units by the relation $\omega_{0P}^2 = 1 + k_{0P}^2$, from which $k_{0P} = 3.0185$. For the stimulated Raman scattering, or the coupling of a pump light wave to a daughter scattered light wave and an electron plasma wave, the values of the electron plasma wavenumber k_{eB} associated with the stimulated Raman backscattered mode SRBS, and the plasma wavenumber k_{eF} associated with the stimulated Raman forward scattered mode SRFS are roots of Eq. (27), see Bers et al., [26].

$$[(15W/4-6)]K + (\mu+3W-3)K - 2\mu\,[W - 1 + (5/2\mu)^{1/2}K + 2W - 1 - (5/2\mu)(W-1) = 0 \qquad (27)$$

The corresponding frequencies for the SRBS plasma wave and the SRFS plasma wave are solutions of Eq. (28), see Bers et al., [26]:

$$\omega^2 \approx 1 + 3k^2\lambda_{De}^2 / \omega^2 + 15k^4\lambda_{De}^4 / \omega^4 - 5/(2\mu) \qquad (28)$$

We assume an electron temperature T_e = 0.2 keV. In Eq. (27) the parameter $\mu = m_e c^2 / \kappa T_e = c^2 / \upsilon_{te}^2 = 1/(0.04424\sqrt{T_e})^2 = 2555.$ The resulting roots of Eq. (27) are $k_{eB}\lambda_{De}$ =0.09774 for the plasma mode associated with the SRBS, and k_{eF} λ_{De} = 0.0214 for the plasma mode associated with the SRFS. In our normalized units the Debye length $\lambda_{De} = \upsilon_{te}/c = 0.04424\sqrt{T_e}$ (T_e is in keV), so λ_{De} =0.0198 for T_e = 0.2 keV. We finally get $k_{eB} = 0.09774/\lambda_{De} = 4.94$ for the plasma wave associated with the SRBS, and $k_{eF} = 0.0214/\lambda_{De} = 1.0816$ for the SRFS plasma wave.

The corresponding frequencies for the SRBS plasma wave and the SRFS plasma wave are solutions of Eq. (28). We get for the SRBS plasma wave ω_{eB}= 1.0134, and for the SRFS plasma wave ω_{eF} = 1.000. The selection rules give the following results for the forward scattered electromagnetic wave (ω_{0F}, k_{0F}) and the backward scattered electromagnetic wave (ω_{0B}, k_{0B}):

$$\omega_{0B} = \omega_{0P} - \omega_{eB} = 3.18 - 1.0134 = 2.166 \qquad \omega_{0F} = \omega_{0P} - \omega_{eF} = 3.18 - 1.000 = 2.18 \quad (29)$$

$$k_{0B} = k_{eB} - k_{0P} = 4.94 - 3.0185 = 1.9215 \qquad k_{0F} = k_{0P} - k_{eF} = 3.0185 - 1.081 = 1.9375 \quad (30)$$

Note the close values of (ω_{0F}, k_{0F}) with (ω_{0B}, k_{0B}). We verify that the results in Eqs. (29,30) obey the dispersion relation of the electromagnetic wave $1 + k_{0F}^2 = \omega_{0F}^2$, (from which we get ω_{0F} = 2.18), and $1 + k_{0B}^2 = \omega_{0B}^2$, (from which we get ω_{0B}= 2.166. These results are in very good agreement with the results in Eq. (29). We note also the possibility of the anti-Stokes resonance according to the selection rules $\omega_{as} = \omega_{as} + \omega_{eF}$ =3.18 +1.00= 4.18, $k_{as} = k_{0P} + k_{eF}$ = 3.0185 + 1.081 = 4.099.We calculate from the dispersion relation for the electromagnetic wave $1 + k_{as}^2 = \omega_{as}^2$ a value ω_{as} = 4.219 ,very close to the value of 4.18 calculated from the selection rule.

The ions were included in the calculation. They established a small self-consistent sheath at the edges. Their presence belongs to the high and low frequency kinetic instabilities which can occur when modified distribution functions exist during the evolution of the system as we mentioned before. Also a contribution of the ions in the scattering of the waves will be discussed at the end of this section 3. We use a fine resolution grid in phase-space, with N = 30000 grid points in space, and 800 grid points in momentum space for the electrons (extrema of the electron momentum are ±1.2 . We have initially a flat profile of a uniform plasma slab with the normalized density n_e=n_i=1. This flat profile of the uniform plasma extends over a length $L_p = 570.8c/\omega_{pe}$. On either side of the initial plasma slab the densities are smoothly brought down to zero through an initial parabolic profile of length $L_{edge} = 8c/\omega_{pe}$. An extra vacuum region of length $L_{vac} = 6.6c/\omega_{pe}$ exists on each side of the slab, for a total length of the system of $L = 600c/\omega_{pe}$. In our normalized units $\Delta x = \Delta t = 0.02$, very close to the Debye length λ_{De}= 0.0198.

We first verify the forward propagating linearly polarized pump wave is injected in the domain at the left boundary at x=0 with $E^+ = 2E_{0P}\cos(\omega_{0P}t)$, $E_{0P} = \omega_{0P}a_{0P}$, with a_{0P} = 0.04 . The pump precursor reaches the right boundary at t=600 (since in our normalized units x=t), as can be verified in Figure (1A). At that time a seed pulse is injected at x=L in the backward direction in the form $E^- = -2E_{0B}P_{0B}(t)\cos(\omega_{0B}\tau)$ where ω_{0B} = 2.166 and $\tau = t - t_1$. The temporal shape factor of the seed pulse is $P_{0B}(t) = \exp(-0.5(t-t_0)^2/w^2)$ with $w = \tau_s$ =6.2, t_2=600, t_2=600 , t_0=580, t_1=560, $t_1 < t < t_2$. $E_{0B} = \omega_{0B}a_{0B}$, with a_{0B} = 0.01318. In this way the seed Gaussian pulse starts penetrating the domain from the right boundary at t=t_1=560. When the pump precursor has reached the right boundary x=L=600 at t=600, the seed pulse has fully penetrated from the right boundary, and its peak has reached the point at x=580 at the time t=620.

For the parameters used in this simulation, the SRFS plasma mode with $k_{eF}\lambda_{De}$ =0.0214 is very weakly damped. No seed or initial perturbation is added to stimulate the more damped SRBS mode with $k_{eB}\lambda_{De}$ =0.09774. We present in Figures (1B) the evolution of the incident pump E^+ wave (full curve) and the backward seed pulse E^- (dashed curve) at: a) t=820, b) t=920, c) t=1160, d) t=1220. The growth and contraction of the seed pulse (dashed curves), propagating towards the left, is obvious, and also the detachment of the front of the growing seed pulse. The constant amplitude full-curve at the left is for the constant amplitude incident pump. Once the seed is reaching the same amplitude as the pump, we enter the regime of pump depletion. The smaller peaks we see behind the front pulse of the growing seed are due to the fact that when the pump depletes, the seed pulse can loose energy again for the pump, which results in the oscillations in the tail of the seed we observe (*i.e.* the amplified seed beats with the plasma wave to regenerate the pump, which results in a local depletion of the seed). Also, the exchange with the anti-Stokes resonance can play a similar role in this oscillation.

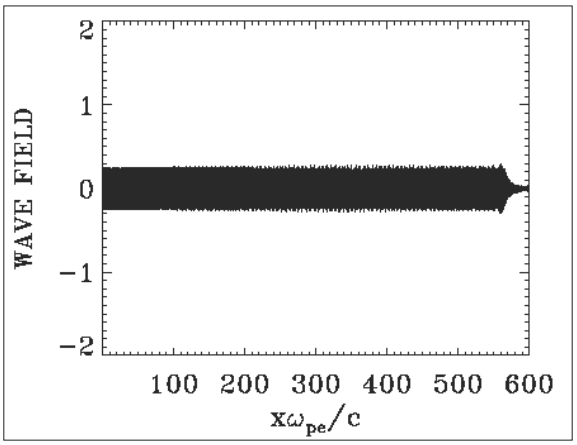

Figure 1A: The Incident Pump E^+ at t=600. The Pump Precursor is reaching the Right Boundary.

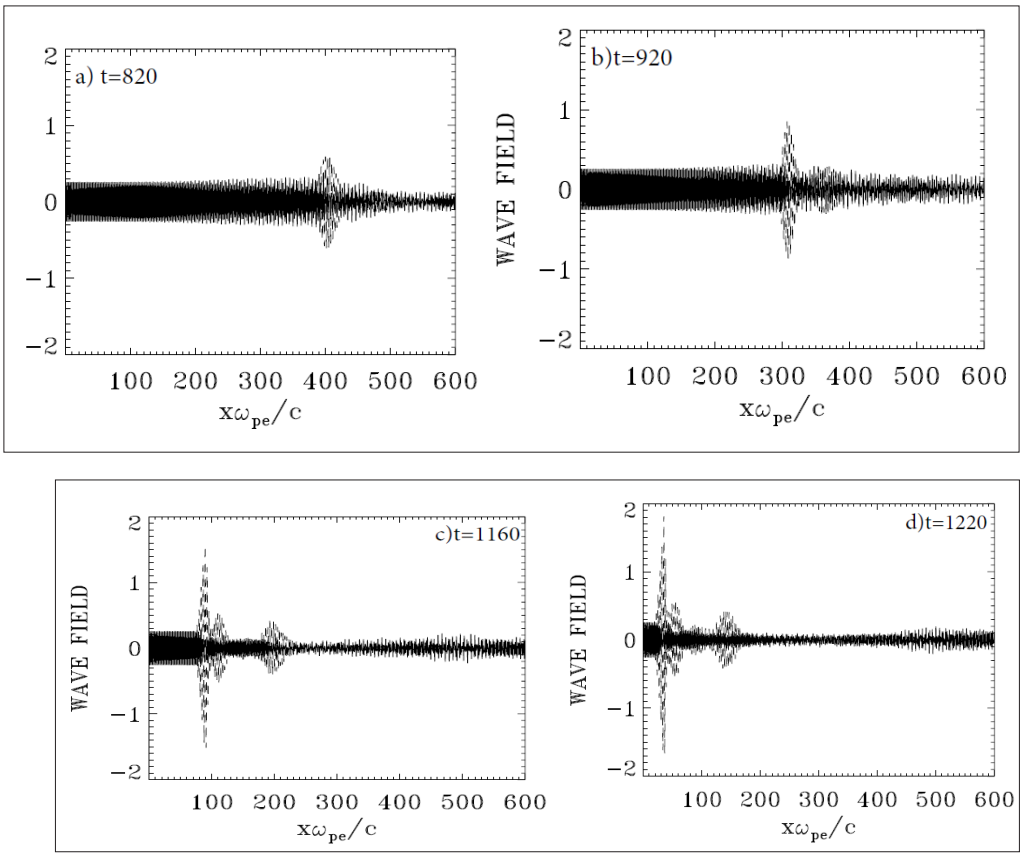

Figure 1B: The Evolution of the Incident Pump E^+ Wave (Full Curve) and the Backward Seed Pulse E^- (Dashed Curve) at :a) t=820, b) t=920, c) t=1160, d) t=1220; and a_{0P} = 0.04.

We present in Figure (2) a plot of the electron density at t=1160 and t=1220, corresponding to Figure (1Bc,1Bd), and in Figure (3) the electron density in the region of the front edge in $x\in$ (15,65) at t=1220. We observe regular oscillations in the front edge in $x\in$ (15,65), where the growing backward seed pulse is dominating. The wavelength associated with these regular oscillations is the wavelength of the plasma wave associated with the growing seed pulse, which is $\lambda_{eB} = 2\pi / k_{eB}$ =1.27. We shall see below that this corresponds to coherent vortical structures in phase-space, while the part of the density plots in Figure (2) which shows a rather noisy density profile to the right of the growing seed pulse, corresponds to a region in phase-space where vortices were actively merging.

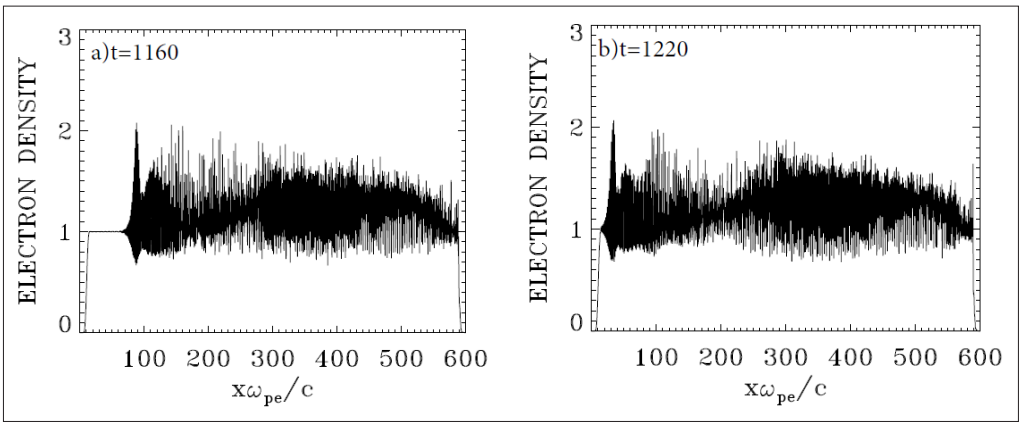

Figure 2: Plot of the Electron Density Profile at t=1160 and t=1220; and a_{0P} = 0.04

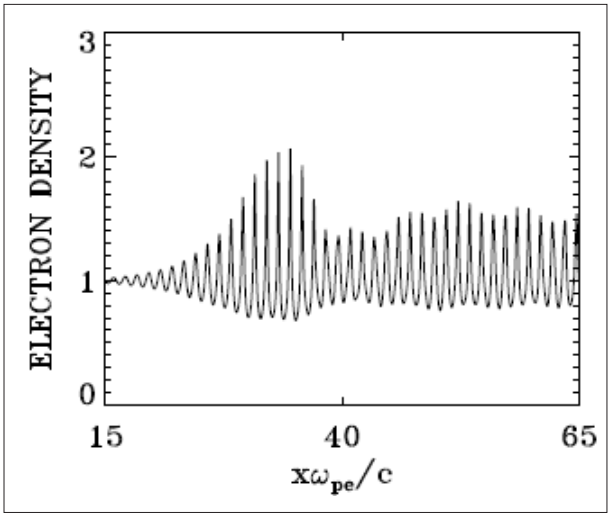

Figure 3: Plot of the Electron Density in the Region of the Front Edge in $x\in$ (15,65) at t=1220.

This is also shown in Figure (4), where we present in the phase-space the contour plots of the electron distribution function in $x\in$ (15,65), and in $x\in$ (65,115) at t=1220. In $x\in$ (15,65) we observe a coherent vortices structure associated with the plasma wave corresponding to the growing seed pulse (see the profile in Figure (3)), while in $x\in$ (65,115) we see the vortices at the right of Figure (4) who are coalescing together, leading to the somewhat noisy structure we see at the right the density plots in Figure (2)

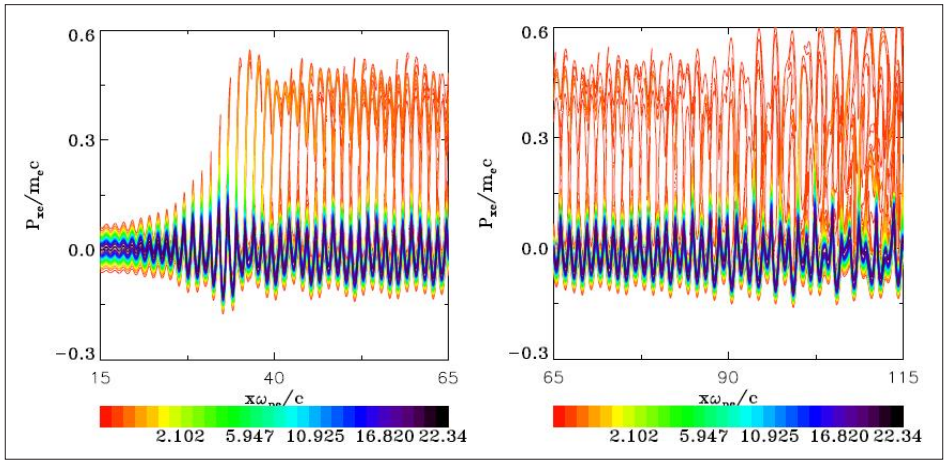

Figure 4: Phase-space Plot of the Electron Distribution Function in $x\in$ (15,65) and in $x\in$ (65,115)

3A Verification of the Response of the Code before the Interaction of the Pump Wave with the Seed Pulse Wave in the Case of the Stimulated Raman Backscattering

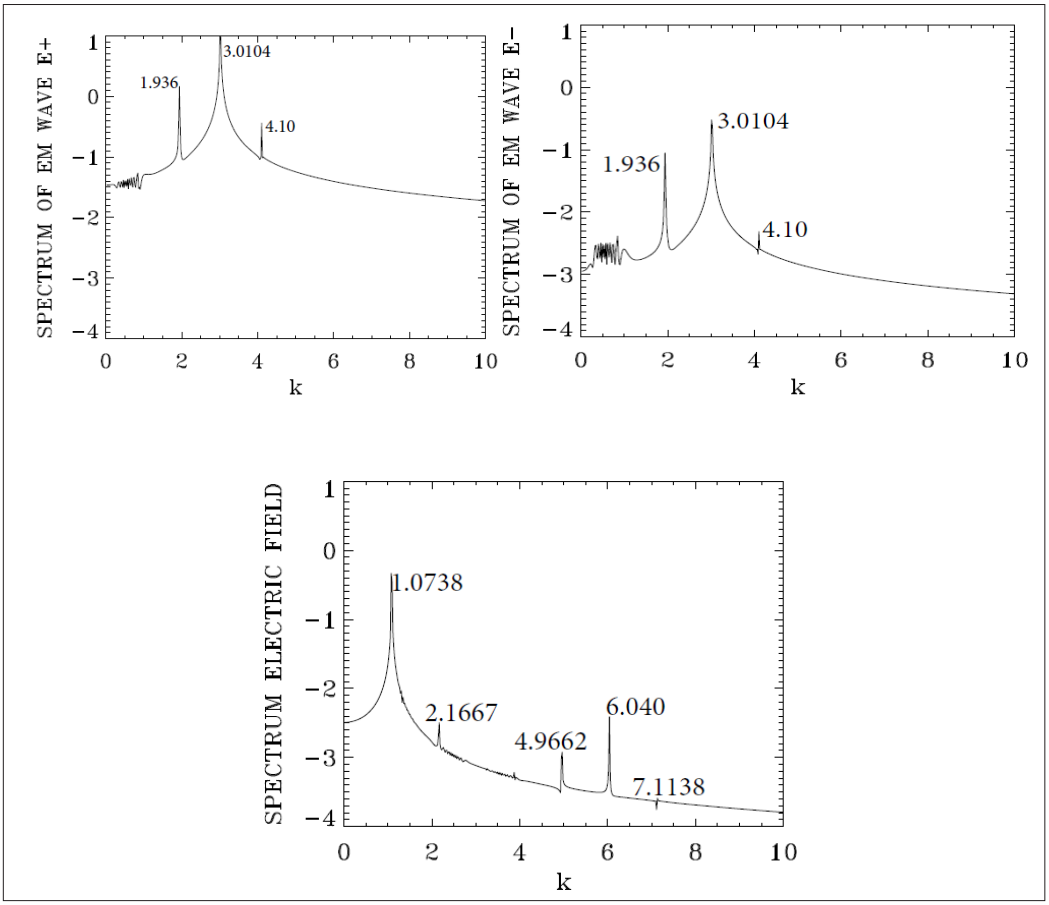

Figure 5: Wavenumber Spectra of (Clockwise) the Incident Wave E^+, the Backward Wave E^- and the Longitudinal Electric Field E_x in the Domain $x\in$ (140,468) at time t=640.

We present in Figure (5) the wavenumber spectra of the incident wave E^+, the backward wave E^- and the longitudinal electric field in the domain $x\in$ (140,468) at the time t=640, well before the backward injected seed reaches this part of the domain, see Figure (1). The only excited waves in this case are due to the forward propagating pump E^+. We recognize the peak of the pump E^+ at k_{0P}=3.01 (verified at 3.0184 in our theoretical calculations in Eq. (30)). The pump is exciting a weakly damped, forward propagating wave with wavenumber k_{0F} = 1.936 , in agreement with our theoretical results in Eq. (30). We have also a very small peak for the anti-Stokes wavenumber at k_{as} = 4.1034 (calculated at 4.099 in our theoretical calculations following Eq. (30)). Since the plasma is a nonlinear medium, the same modes are appearing in the spectrum of the backward wave E^- at a much lower amplitude. The wavenumber spectrum of the excited longitudinal electric field shows the wavenumber of the resonant plasma mode for the forward wave at k_{eF}=*1.0738* (calculated at 1.081 in our theoretical calculations). The values of k_{0B} and k_{0F} in Eq. (30) are very close. The pump wave at 3.0104 in the spectrum of E^+ in Figure (5) can couple with the backward mode at 1.9366 in the spectrum of E^- to produce the plasma mode at 3.0104= –1.9366 + k_{keen}, or k_{keen}= 4.977 , very close to the calculated plasma wave k_{eB} = 4.94 associated with the backscattered Raman wave (the spectrum of the longitudinal electric field shows a peak at 4.966 in Figure (5)). So even though the seed pulse is still far away, there is a small plasma mode at 4.966 excited well before the arrival of the seed pulse, associated with the backward resonance due to the coupling of the pump at k_{0P} = 3.0104 in E^+ (which is exciting the forward scattered mode at k_{0F} = 1.936), with the backward mode appearing at 1.936 in the spectrum of E^- in Figure (5). So the pump is exciting the plasma mode around 4.96 through two backward resonances. A backward resonance taking place with the wave 3.0104=-1.936+4.977, and will excite it again in the future resonance with the backward seed pulse, which still did not take place in the spectra in Figure (5) at t=640. Finally for the linearly polarized wave, we have a plasma mode appearing in the spectrum of the longitudinal wave at the harmonic of the pump $2k_{0P}$ = 6.04 (calculated at 6.036 from our theoretical results k_{0P} = 3.0185).

Indeed, for the linearly polarized wave, we have a plasma mode appearing at the harmonic of the pump $2k_{0p} = 6.04$. This is due to the fact that if we have a linearly polarized wave: $\vec{E} = (0, E_y, 0)$, we can write in a linear analysis with $E_y = E_0 \cos(\psi)$, $\psi = (kx - \omega t)$ using Faraday's law:

$$\frac{\partial \vec{B}}{\partial t} = (0,0,-\frac{\partial E_y}{\partial x}) \qquad (31)$$

Then $\vec{B} = (0,0,B_z)$ with $B_z = B_0 \cos(\psi)$, and $B_0 = E_0 k/\omega$. From $\vec{E}_\perp = \hat{e}\ \vec{a}_\perp / \partial t$ Eq. (11), and $\vec{p}_\perp = \vec{a}_\perp$, we get $\vec{p} = (0, p_y, 0)$, with $p_y = -p_0 \sin(\psi)$, and $p_0 = E_0/\omega$. The longitudinal Lorentz force is $p_y B_z = -\frac{1}{2} k p_0^2 \sin(2\psi)$. This drives a longitudinal response at the harmonic of the laser wave.

The forced oscillations at the wavenumber 6.04 further stimulates the mode at 4.966, by coupling with the plasma wave at 1.0738, through the selection rule 6.04=4.966+1.0738. Also, a longitudinal plasma mode appears at the wavenumber 7.1138 through the coupling 7.1138=6.040+1.0738, seen in Figure (5) in the spectrum of the longitudinal electric field. We have here a cascade of coupling of plasma waves, very nicely verified by the numerical code.

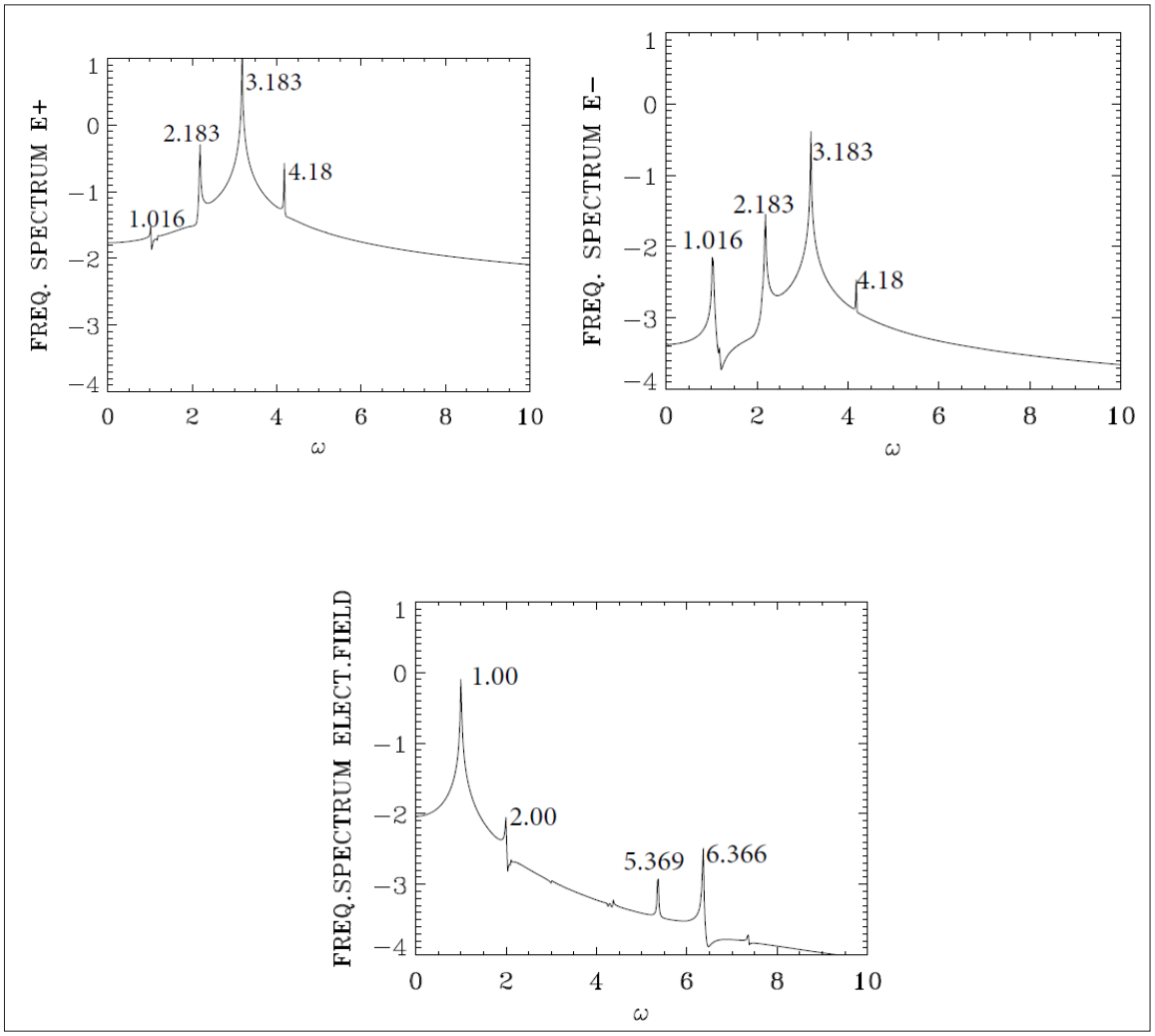

Figure 6: Frequency Spectra of (Clockwise) the Incident Wave E^+, the Backward Wave E^-, and the Longitudinal Electric Field Ex, at the Position x=150, at Time t=(192,819).

We look now at the frequency spectra of the excited modes before the arrival of the growing backward seed pulse. Figure (6) presents the frequency spectra of the pump wave E^+, the backward wave E^- and the longitudinal electric field, from the data recorded at the position x=150 between t_1=492 and t_2=819, before the arrival of the backward propagating seed pulse. The spectrum of E^+ in Figure (6) shows the pump frequency at 3.183 (calculated 3.18 in Eq. (29)), the forward Raman scattered mode SRFS at 2.183 (calculated at 2.18 in Eq. (29)). The anti-Stokes mode is at 4.18 (calculated at 4.18 following Eq. (30)). These same modes appear in the spectrum of E^- in Figure (6) as previously explained, since the plasma is a nonlinear medium. We see a mode at frequency 1.00 in the frequency spectrum of the longitudinal electric field excited through the forward coupling of the pump frequency SRFS at 3.183 with the forward scattered mode of 2.183, and with the plasma wave of frequency 1.0, 3.183=2.183 +1.00. We also see the plasma wave at the harmonic of the pump $2\omega_{0p}$ = 6.366 as explained in Eq. (31). And the coupling of the pump at 3.183 with the wave at

(ω_{0F}, $-k_{0F}$) produces a Keen wave, with frequency 3.183= 2.183 + ω_{keen}, from which ω_{keen} = 1.00. So the plasma frequency of 1.0 is produced by the coupling of the pump 3.183 plasma wave with the forward scattered mode at 2.183 and by the coupling of the pump wave with k_{0F} = -2.183, which produces a Keen wave of frequency 1.0, as discussed at the end of the first paragraph in this section 3A. We note also the mode at the plasma frequency 5.369 which can be excited through the forced oscillation 1.00+5.369=6.369, very close to the forced oscillation at 6.366. We also note in Figure (6) the possible further forced resonance 3.183+2.183=5.366, very close to the plasma mode at 5.369. There is an important collection of modes excited other than the SRBS and SRFS modes, even before the arrival of the growing backward seed pulse. And the code is giving a nice resolution of these modes, in the absence of numerical noise, with a very interesting agreement between the theoretical predictions of the selection rules and the numerical calculation from the simulation code.

3B Study of the Response of the Code during and after the Interaction of the Pump Wave with the Growing Seed Pulse Wave in the Case of the Stimulated Raman Backscattering

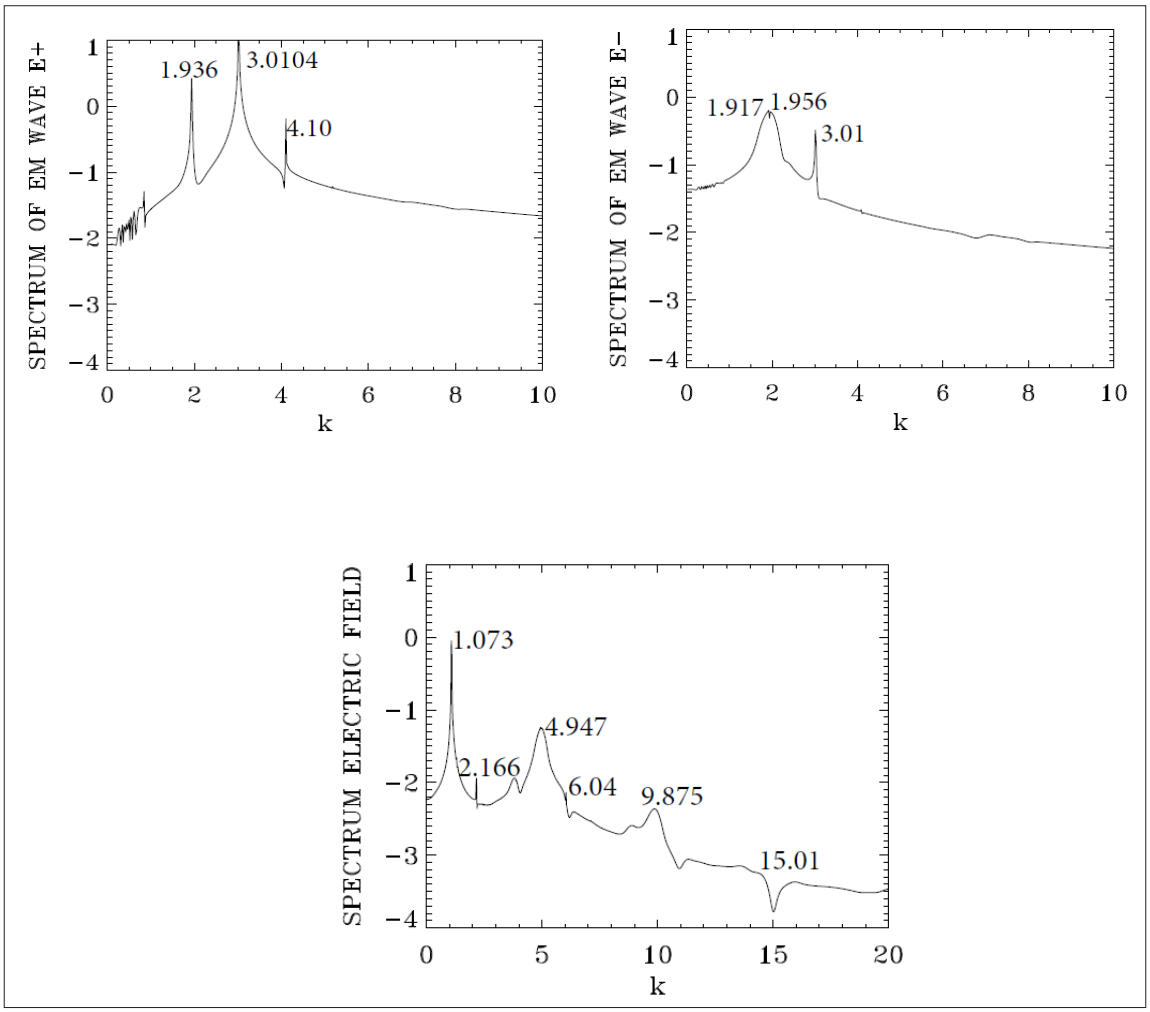

Figure 7: Wavenumber Spectra of (Clockwise) the Incident Wave E^+ , the Backward Wave E^- and the Longitudinal Electric Field E_x in the Domain $x\in$ (140,468) at Time t=740.

We look again in Figure (7) to the wavenumber spectra in the same domain $x\in$ (140,468), the same domain we studied in Figure (5), but at the time t=740, when the backward pulse has entered now the domain $x\in$ (140,468), see Figure (1). The spectrum of E^+ is essentially the same as in Figure (5), however the mode at 1.936 is more stimulated. The spectrum of the backward wave in E^- in Figure (7) shows the effect of the arrival of the pulse. There is a broad peak. We are still in a transient phase, and this broad peak is due to the presence of the mode at 1.936 which results from the forward coupling of the pump 3.010=1.936+1.074 (the mode wavenumber in the spectrum of the longitudinal electric field in Figure (7) appears at 1.073). There is a wavenumber coupling 3.010=—1.936 +k_{keen}, from which we can identify the kinetic mode at k_{keen} = 4.946, which we see in the spectrum of the longitudinal electric field in Figure (7). Finally the frequency of the arriving backward seed pulse from Eq. (29) is at ω_{0B} = 2.166 , and should result in a wavenumber response in E^- at k_{0B} = 1.921 (precisely in the broad peak we observe in the spectrum of E^- in Figure (7)), and in a wavenumber of the longitudinal electric field at k_{eB} = 4.94 (see again the broad peak in Figure (7)). So, the peak at 4.947 results from the excitation of the wave at wavenumber k_{keen} = 4.946 discussed few lines above, and of the plasma wave response to the SRBS wave at k_{eB} = 4.94 . See also the growing harmonic at 9.894 of the plasma mode at 4.947, in the spectrum of the longitudinal electric field in Figure (7).

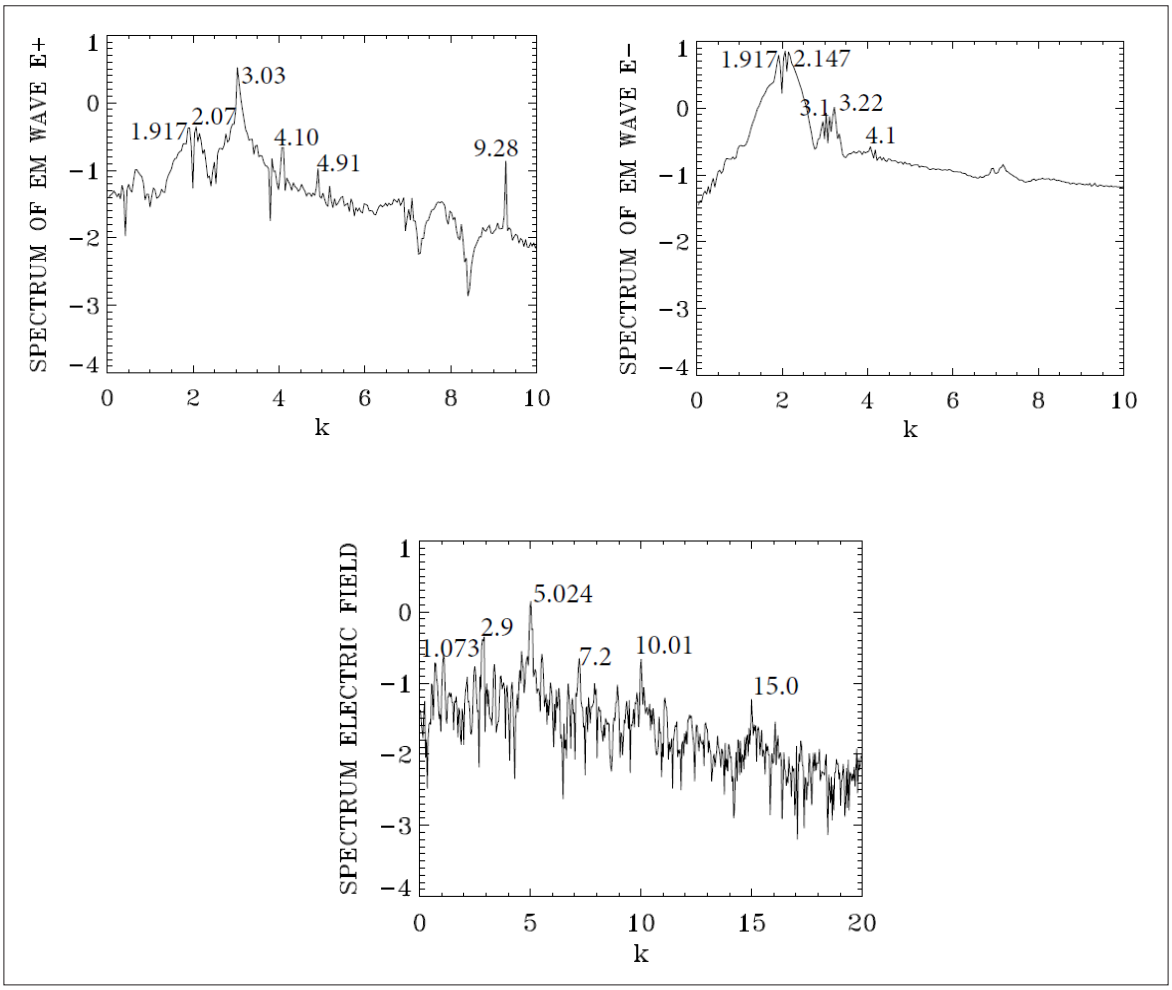

Figure 8: Wavenumber Spectra of (Clockwise) the Incident Wave E^+, the Backward Wave E^- and the Longitudinal Electric Field E_x in the Domain $x\in$ (30,194) at Time t=1220.

Figure (8) presents the wavenumber spectra at the end of the simulation at t=1220, in the domain $x\in$ (30,194). The peak of the pump is now at 3.03 in the spectrum of E^+, also appearing in a broad spectrum around 3.1 in the spectrum of E^- in Figure (8). The dominant mode is now in the spectrum of the amplified backward seed in E^-, where we see in Figure (8) a broad spectrum between 1.917 and 2.147 (these are peaks of the backward seed wave initially calculated at 1.921, and the peak at 1.937 identified as a backscattered wave as discussed for the spectrum of E^- in Figure (7)). These two peaks are appearing also at 1.917 and 2.07 in the spectrum of E^- in Figure (8). These are also analogous to the broad double peaks we observe in the spectrum of in Figure (7), due to the backscattered Raman wave and the backscattered Keen wave. The anti-Stokes at $k_{as} \approx 4.1$ is also present in E^+ and E^-. The spectrum of the longitudinal electric field in Figure (8) shows the peak of the plasma wave associated with the forward Raman scattering at k_{eF} = 1.073 (calculated at 1.081 in our theoretical results from Eq. (30)). Also the plasma wave at k_{eB} = 5.023 associated with the backward Raman scattering (calculated at 4.94 in our theoretical results in Eq. (30)), and the scattering of the pump wave at 3.03 with the mode at 1.97 in the spectrum of E^-, which results in a Keen wave 3.03=-1.917 + k_{keen} , from which k_{keen} = 4.947.

The frequency spectra we present in Figure (9) are calculated by monitoring the fields at the position x=150, for the values of time $t\in$ (1050,1214) , after the arrival of the growing backward seed pulse. The theoretical value of the pump frequency at $\omega_{0P} = 3.18$ is appearing in the frequency spectrum of E^+ in a broad peak around 3.144. The frequency spectrum is now dominated by the growing backward seed wave, we see a broad peak around 2.147 and 2.3 in the frequency spectrum of E^- (theoretical values calculated in Eq. (29) are for the backscattered Raman wave at 2.166 and for the backscattered Keen wave at 2.18). These peaks are also present in the frequency spectrum of E^+ around the peaks at 2.186 and 2.3. The dominant E^- wave is now interacting with the pump and shifting frequency at 3.22 in the frequency spectrum of E^-. The anti-Stokes frequency calculated at 4.18 is still at 4.18 in the frequency spectrum of , and appears also around 4.29 in the frequency spectrum of E^-. The frequency spectrum of the longitudinal electric field shows a broad peak at ω_{eB}=1.00. The frequency of the plasma wave associated with the backward Raman scattering is calculated at 1.0134 in our theoretical results. The theoretical value of the frequency of the plasma wave associated with forward Raman scattering is ω_{eF}=1.00. We have in Figure (9) for the longitudinal plasma wave a broad frequency around 1.00, extending to lower values with respect to the plasma frequency, which would denote a variation of the nature of the plasma wave to that of a Keen wave below the frequency of 1.0 [18,20]. Note the multiple harmonics structures in the plasma wave.

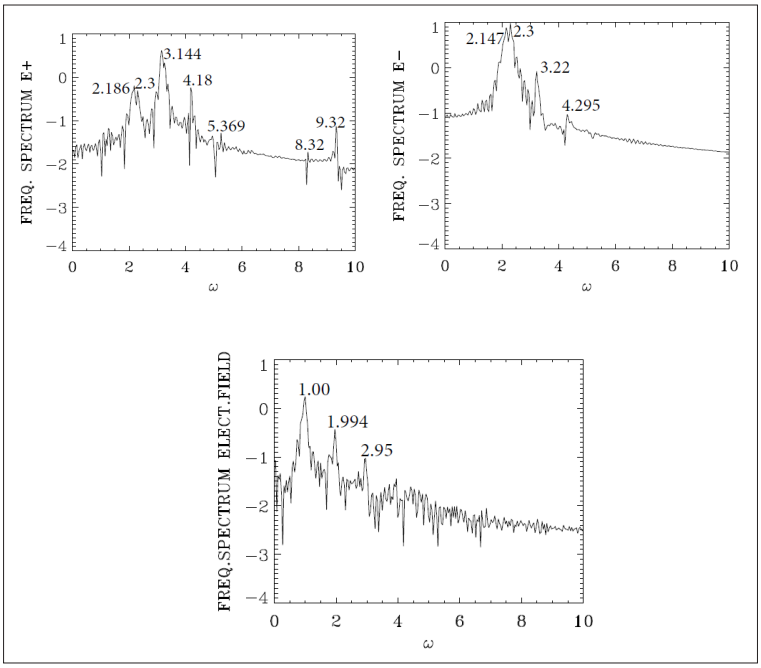

Figure 9: Frequency Spectrum at the Position x=150 for the Time $t\in$ (1050,1214).

We note in the spectrum of E^+ in Figure (8) the mode at k_{0F} =1.917, also appearing in a broad spectrum around k_{0B}= –1.917 in the spectrum of E^- in Figure (8). These two opposing modes can give a Brillouin scattered mode in the forward direction. We verify in the ion density plot in the Figure (10) below a plot of the ion density at t=1220. The growth in these ion oscillations starts around x=100, which is just behind the position where the peak of the growing backward seed wave is reaching a high peak close to the left boundary, as we can verify from Figure (1B). During the growth of the backward seed wave, the SRBS mechanism dominates when the growing high seed peak at –1.917 of is dominating. Behind this front region, the forward pump wave at 1.917 and the seed are competing together. This result in an exchange of energy between the modes which we see appearing behind the peak wave crest in Figure (1). We have in the spectrum of in Figure (8) the mode at k_{0F} =1.917, also appearing in a broad spectrum around k_{0B}=-1.917 in the spectrum of in Figure (8), we can write the relation $k_{0F} = k_{0B} + k_{ip}$ from which k_{ip}=2*1.917 =3.834, which is the peak we see in the spectrum of the ions density in Figure (10), together with its harmonics. We can verify from Figure (10) that for a distance x less than 100, the stimulation of the backward Raman activity with a clear dominant growing seed pulse, while behind the growing seed pulse for a distance x greater than 100 a forward Brillouin scattering activity is developing, where we verify in Figure (1B) at t=1220 an oscillation appearing for x greater than 100 which is the results of an exchange of energy between at k_{0F} =1.917, and between at k_{0B}= –1.917, which results in a forward Brillouin scattering activity which we see in Figure (10) at k_{ip}=2*1.917. This is interesting to note, since in a PIC code, the low frequency of the Brillouin scattering would have been covered with the numerical noise of the PIC code. The observation of the fact the forward Brillouin scattering seems to originate around x=100 in opposite direction deserves some more attention in future simulations. We note the importance of including an equation for the ions in this problem.

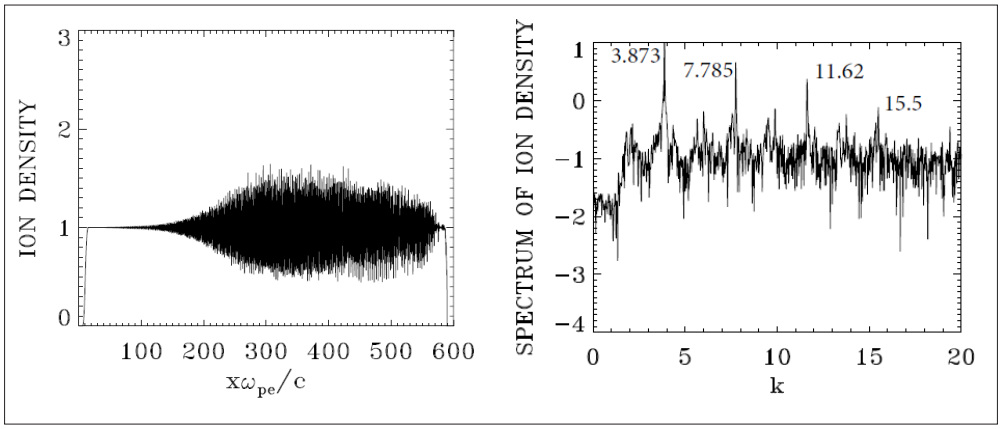

Figure 10: Plot of the Ion Density and the Wavenumber Spectrum of the Ion Density at t=1220.

So far, we have seen how the absence of noise in the Eulerian Vlasov code developed for the relativistic Vlasov-Maxwell equations allows a good resolution of the modes excited by the stimulated Raman backscattering for the amplification of seed pulses in a plasma. We evaluated the response of the code first to the forward propagating pump wave in section 3A. A very nice agreement was verified with the predicted waves response in the system. Usually in the stimulated Raman backscattering for the amplification of seed pulses in a plasma, this response follows the evolution of the electron population. However, section 3B is presenting for the first time interesting details on the amplification of a Brillouin forward ion wave which is generated as shown in Figure (10) at the point around x=100 where it couples with the stimulated Raman backscattered seed pulse, as can verified from Figure (2) and (3). A result which invites to more investigation in the study of the amplification of the stimulated Raman backscattering. In both sections, contributions from kinetic Keen waves have been identified.

4. Simulation of the Seed Pulse Amplification in Plasmas by Stimulated Brillouin Backscattering

We present in this section a numerical simulation using a Eulerian Vlasov code to study the problem of the amplification of seed pulses by Brillouin backscattering in an overdense plasma. In this process, there is an energy transfer, mediated by a resonant ion wave, from a long, electromagnetic wave pump, to an initially counter-propagating ultra-short seed pulse. The code solves the one-dimensional relativistic Vlasov-Maxwell set of equations, and has been presented in Section 2, and has been previously applied to study problems of Brillouin backscattering amplification of seed pulses in plasma [19]. In the study we presented in Shoucri et al., we used the Vlasov code for a length of the system of $1000c/\omega_{pe}$ [19]. For such a length of interaction, in the PIC simulations (Humphry et al.,), the pump becomes depleted due to scattering from numerical noise. The results presented in Shoucri et al., allowed a complete solution of the problem, identifying the modes excited and the growth of the seed pulse [19]. Detailed contour plots of the distribution functions are also presented. In the study we present here, we use the parameters which have been used in Humphry et. al., and in Shoucri et al., but we increase the plasma length from the value of $1000c/\omega_{pe}$ to $1600c/\omega_{pe}$ [19]. We present simulation results in the plateau of a uniform plasma where density is normalized to 1.0, The ratio of the pump frequency to the plasma frequency $\omega_{0P}/\omega_{pe} = 1/\sqrt{n/n_{cr}}$, we use n/n_{cr} = 0.3, from which ω_{op}/ω_{pe} = 1.826. The normalized vector potential or quiver momentum of the pump a_0 verify $a_0^2 = I\lambda_0^2/1.368\text{x}10^{18}$, where I is the laser intensity in W/cm^2 and λ_0 the wavelength in microns. For the chosen pump beam intensity W/cm^2, and wavelength $\lambda_{0\,p} = 1.0\mu$m, the pump normalized vector potential is , assumed constant during the simulation. The normalized time and length units correspond to 0.97 fs and 0.29 , respectively. Hydrogen plasma is assumed, with electron and ion temperatures Te=500eV and Ti=50eV. The Debye length is λ_D= 0.0313. With N=50000 grid points in space, we have for the mesh-size Δx = 0.032 , which is of the order of the Debye length. The extrema of the electrons momentum are ±0.4, and for the ions momentum ±10 . We use for the seed pulse an intensity of W/cm^2 at the same wavelength as the pump pulse, which leads to a_{0s} = 0.027 . The backward seed frequency is denoted by is equal to the pump frequency, as is usually the case for the small value of the frequency downshift of the ions in Brillouin scattering, we set $\omega_{0s} = \omega_{0p} = \omega_0$. From the dispersion relation $\omega_{0p}^2 = 1 + k_{0p}^2$ we have for the corresponding wavenumber k_{0p}= 1.528. The dispersion relation of the ion wave is k_{pi} = 2*1.528, the associated wavelength λ_{pi}= 2π/k_{pi} =2.05 This domination of the ion wavelength with λ_{pi}= 2.05 is apparent in Figure (16).

The forward propagating linearly polarized pump laser beam penetrates the plasma at x=0, with a value $E^+ = 2E_{0p}\cos(\omega_0 t)$. Figure (11) show the time evolution of the forward propagating pump, and of the backward propagating growing seed pulse. In the right of Figure (11a), at t=1600, the precursor of the electromagnetic pump has just reached the boundary at x=1600 (x=t in our simulation), while the seed pulse has just penetrated at this boundary (see the small bump at the right, in the Figure (11a)). At time t=1600-2 τ_s, where τ_s = 100 is the duration of the seed pulse, the backward seed wave $E^- = -2E_{0s}\,P_r(t)\cos(\omega_0\tau)$ is injected at the right boundary at x=1600, where $\tau = t - 1400$. The seed pulse has a temporal shape: $P_r(t) = \sin^2(\pi\tau/2\,\tau_s)$, $1400<t<1600$ and zero otherwise. In our normalized units $E_{0p},s = \omega_0 a_{0p},s$. We present in Figure (11b-11d) a sequence showing the growth of the seed pulse which is propagating towards the left. Behind the seed peak, the pump is slowly depleted, while in front of the growing seed pulse, the incident pump maintains a constant amplitude. The simulation is stopped at t=2816 in Figure (11d), due to the formation of a very steep gradient at the seed front, at which point the numerical simulation has been stopped. We have been able to push the calculations further in time compared to the results presented in Shoucri et al., [19]. Comparing Figure (11b) and Figure (11d), we see how the front edge of the growing seed pulse has steepened, compressed, and detached from the tail. Figure (12) and (13) present the electron density and ion density profiles at three different times, while Figure (14) presents the longitudinal electric field. Figure (15) and (16) present the phase-space contour plots at different positions for the electrons and the ions. The domination of the wavelength with λ_{pi}= 2.05 is apparent. Note the excellent performance of the numerical code until the end at t=2816. More details on the phase-space plots and the identification of the modes excited can be found in Shoucri et al., [19].

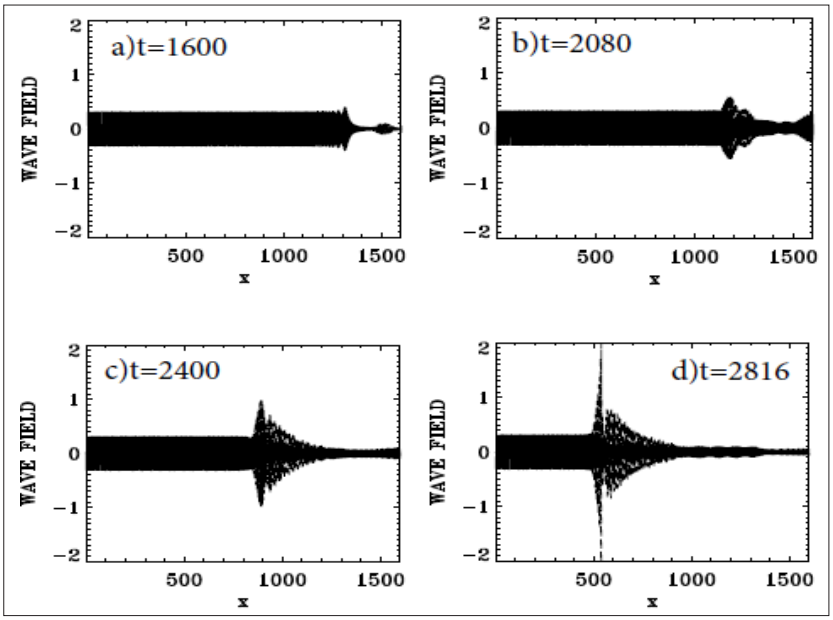

Figure 11: Incident Pump Wave E^+ and the Backward Growing Seed Wave E^- at Different Times.

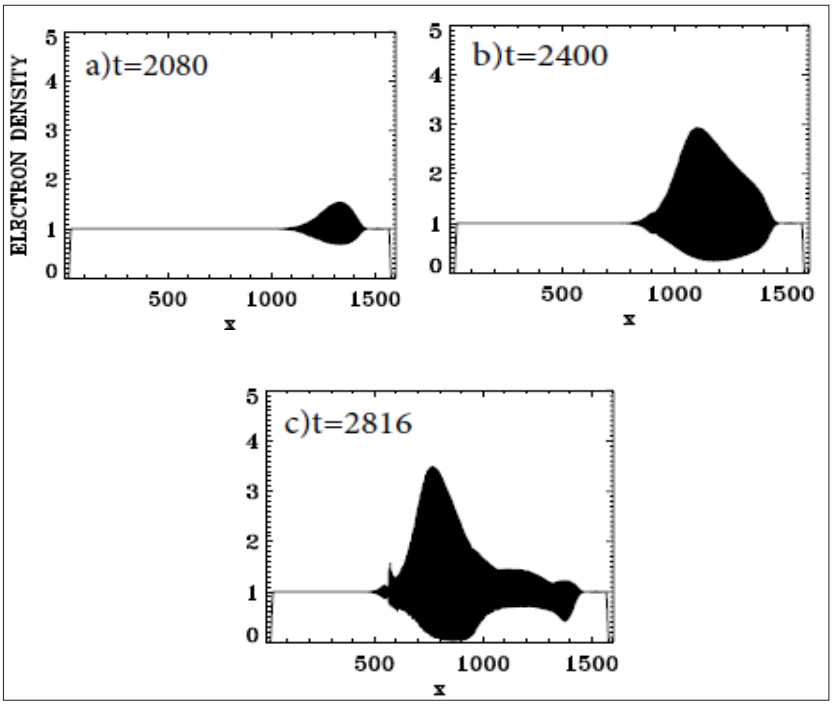

Figure 12: Electron Density Profiles at Different Times

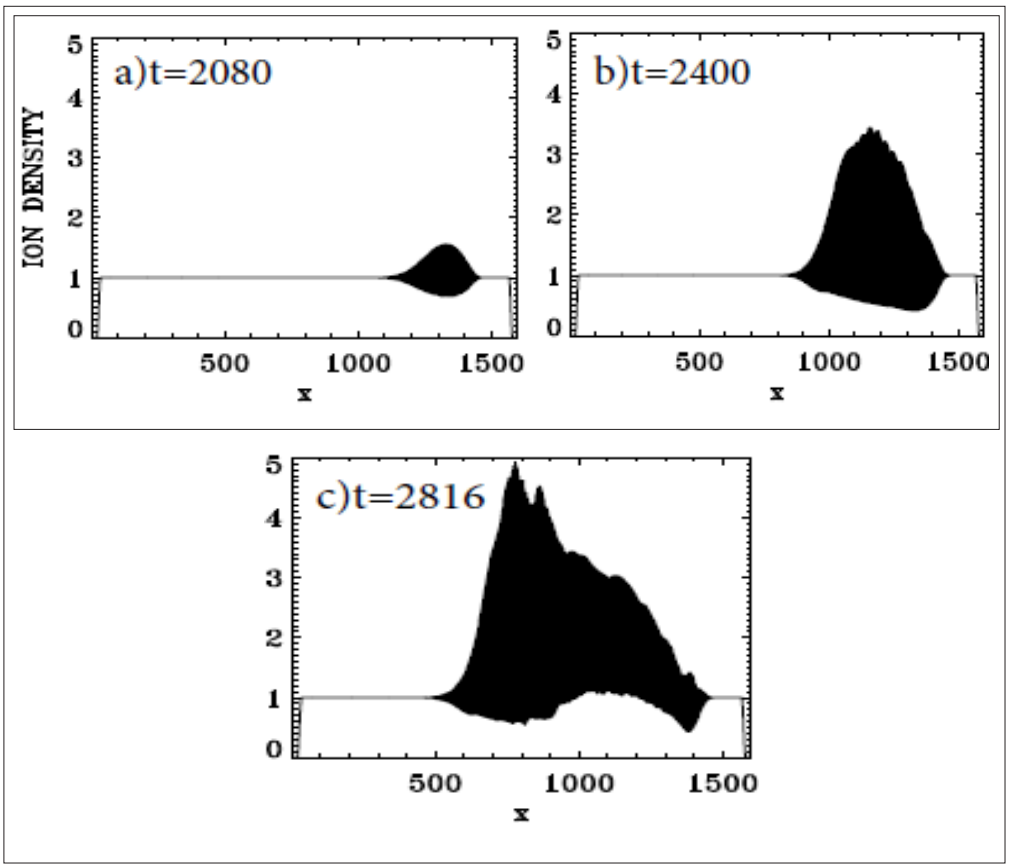

Figure 13: Ion Density Profiles at Different Times

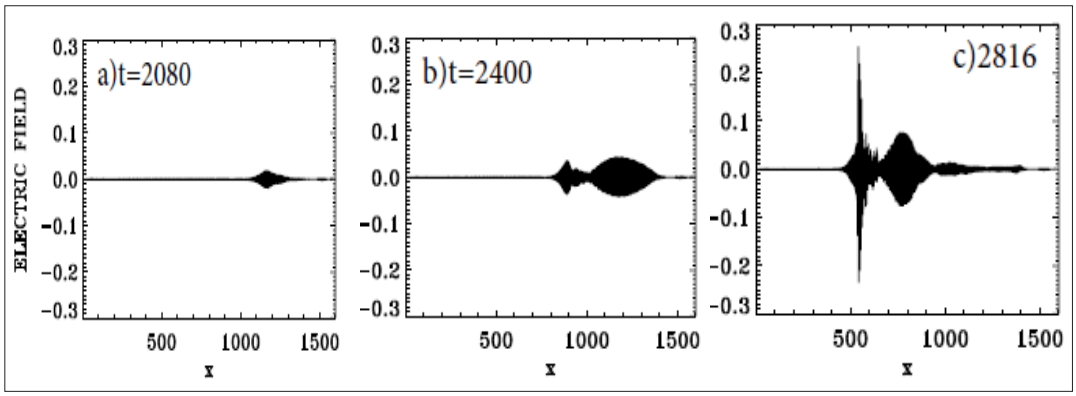

Figure 14: Longitudinal Electric Field E_x at Different Times

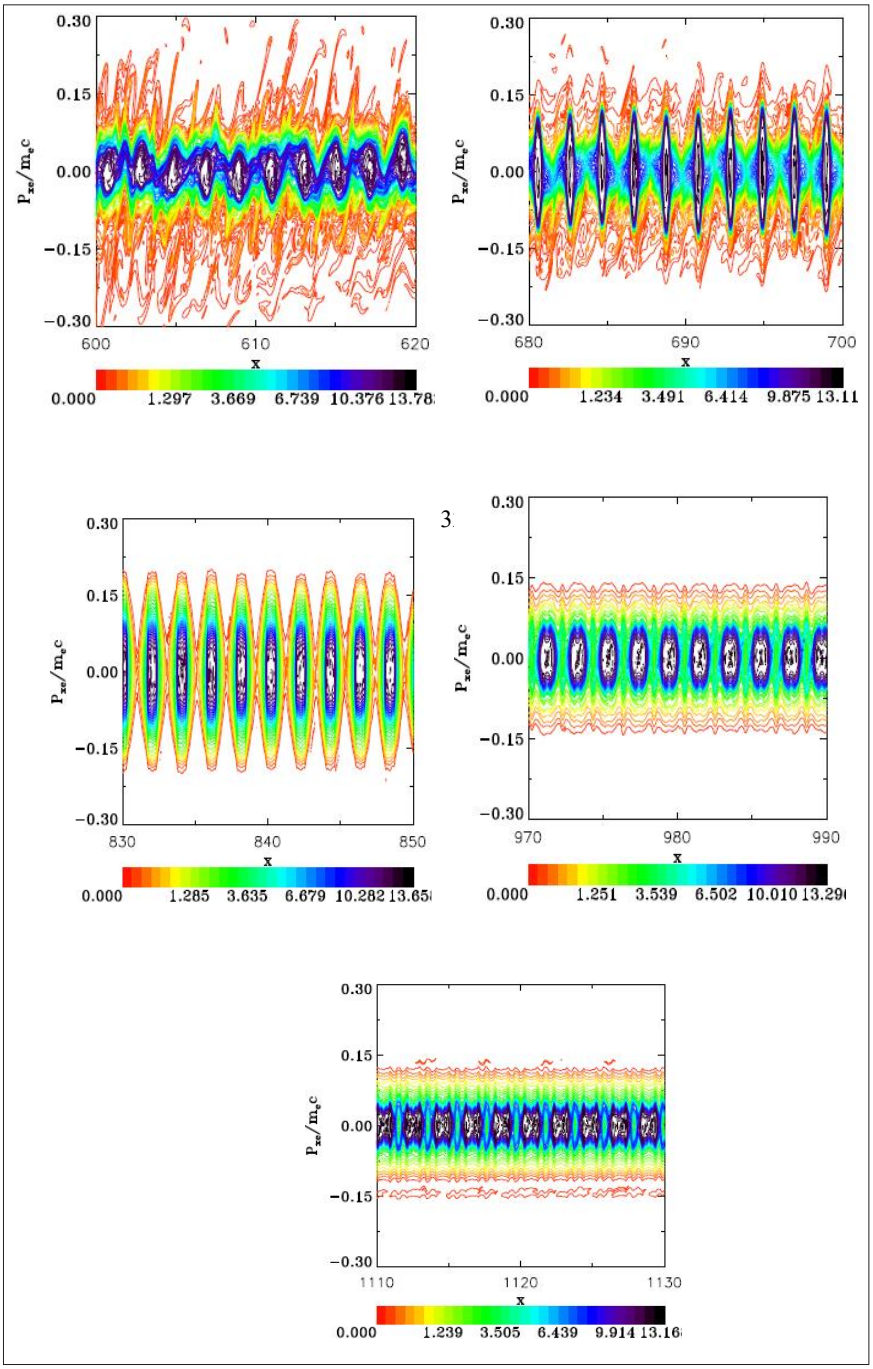

Figure 15: Phase-space Contour Plots of the Electron Distribution Function at *t*=2816.

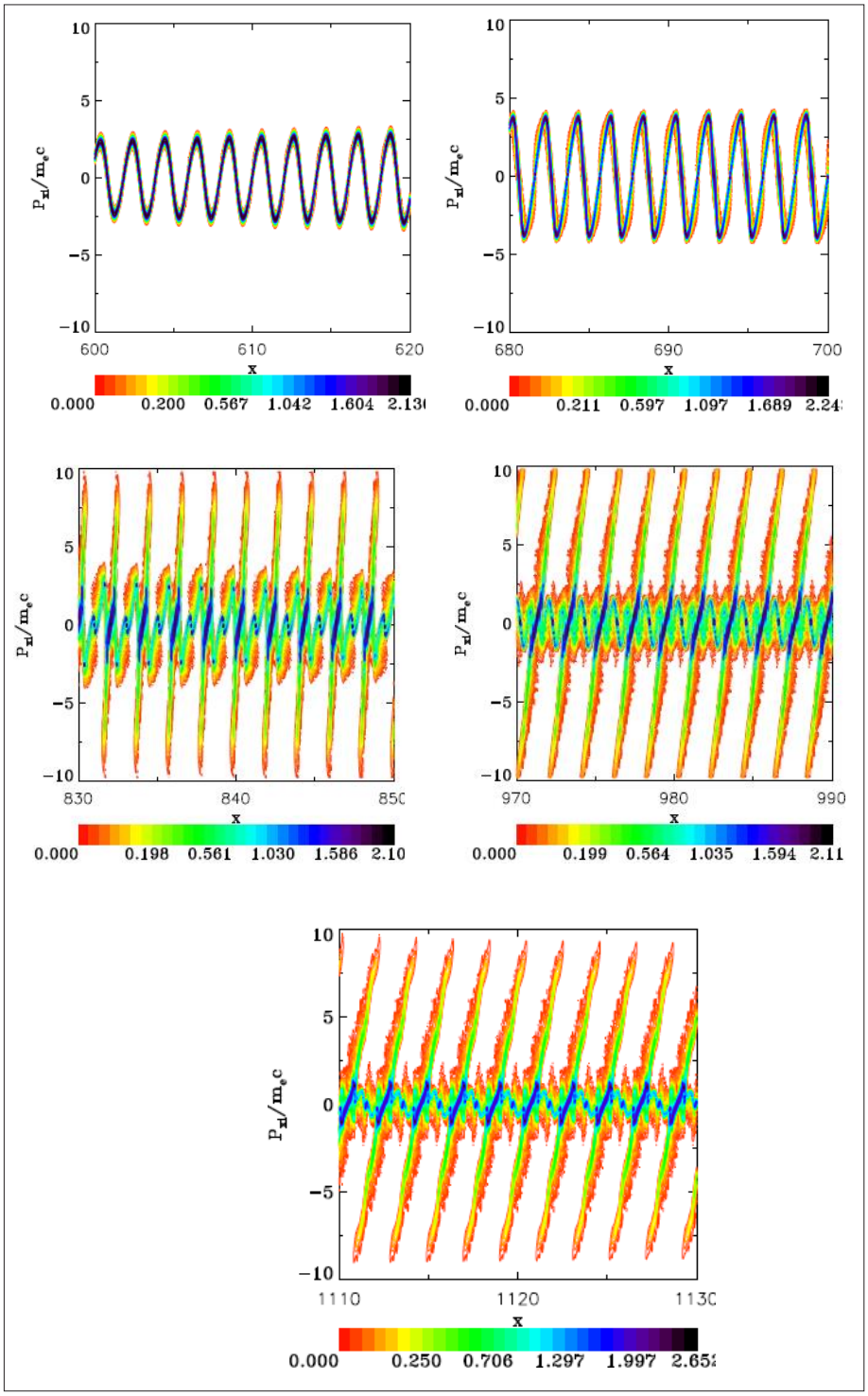

Figure 16: Phase-space Contour Plots of the Ion Distribution Function at t=2816.

In a similar simulation presented in Andreev et. al., the length of the initially uniform plasma system was restricted to $273/\omega_{pe}$ because of the noise level in the PIC simulation makes it impossible to continue the simulation further [27]. In the PIC simulation presented in Humphrey, et. al., the authors added a collision term in an attempt to control but not to eliminate the noise dissipation and excessive pump scattering from the numerical noise, and extended their length to $1000c/\omega_{pe}$, at which time the pump become depleted [28]. In the simulation results presented in Shoucri et al., results with the same numerical code used here were presented for a length of $1000c/\omega_{pe}$. at time t=2033 [19]. At that point, the seed amplitude reached a factor about 6 times higher than that of the pump, or about 20 times the initial seed peak amplitude. We have been able in the present work to push the calculations further in time compared to the results presented in Shoucri et al., [19]. In the results we present in this section, we use the parameters which have been used in Shoucri et al., Humphrey et al., Andreev et al., but we increased the plasma amplifier length to the value of $1600c/\omega_{pe}$, without any numerical noise, about 6 times the

length of $273c/\omega_{pe}$ used in Andreev et al., [19,27,28]. Here, the noiseless Eulerian Vlasov code allows to follow the amplification of the seed pulse by Brillouin backscattering, until the formation of steep gradients of the amplified pulse makes the grid resolution of the steep gradient cannot be resolved anymore. The pump is running until x=1600 when the precursor of the pump reaches the right boundary as we can verify in Figure (11a), at which time the growing seed pulse starts running backward from 1600 down to x= 500, a distance of 1100, see Figure (11). In the simulation results presented here, the plasma amplifier simulation length is extended to $L_p = 1600c/\omega_{pe}$, and the seed pulse amplification was followed until t=2816, at which time contour plots of the distribution functions and derails of the solution are presented with precision. We are presenting here a substantial increase in physics and numerics compared to several simulations previously reported for similar problems.

Conclusion

We have presented in this work an application of a Eulerian Vlasov code for the numerical solution of a one-dimensional relativistic Vlasov-Maxwell equations to study in plasmas, via stimulated Raman backscattering, the problem of the amplification of an ultra-short seed pulse presented in section 3, and the problem of the amplification of an ultra-short seed pulse via stimulated Brillouin backscattering presented in section 4. In both cases the amplification results from the interaction with a long pump pulse assumed to have an envelope that is constant in amplitude before interaction, and mediated by a plasma wave in the SBRS case, or by an ion acoustic wave in the case of a SBBS.

In section 3A detailed analysis of the response of the system to the pump wave before the interaction with the backward seed pulse has been presented, and in section 3B a similar study is presented during and after the interaction of the growing seed pulse with the pump wave via the stimulated Raman backscattering. Comparison between theoretical predictions and numerical simulation results show very nice agreement with available theoretical results. Detailed analysis of the spectra developed during the amplification process are presented, together with the evolution showing the pump depletion, accompanied by the counter-propagating seed-pulse amplification, compression and increased steepness of the waveform. Besides the accurate verification by the numerical code of the predicted theoretical modes, the numerical code shows some modes excited other than the SRBS and SRFS modes as seen in section 3A, even before the arrival and interaction of the backward seed pulse. These modes result from the different coupling of excited modes, and the code is giving a nice resolution of these modes, in the absence of numerical noise. Of these we have pointed to what we have called kinetic electrostatic electron nonlinear Keen waves. These kinetic Keen waves are not steady state, time-independent solutions, but rather transient evolving modes associated with the transient evolution of the distribution function. The absence of noise in the Eulerian Vlasov codes allows accurate identification of the modes involved in the physics of the scattering processes, and more accurate representation of the phase-space structures of the distribution function, especially when relevant to the transient evolution of the system. It prevents numerical problems like excessive pump scattering from the numerical noise. More discussions on the kinetic electrostatic electron nonlinear Keen waves in Shoucri et al., [18,20]. Section 3B has presented for the first time interesting details on the amplification of a Brillouin forward ion wave which is generated as shown in Figure (10) at the point around x =100 where it couples with the stimulated Raman backscattered seed pulse, as can verified from Figure (2) and (3) and (10). Again, the identification of this Brillouin forward scattered ion wave has been made possible because of the absence of numerical noise in the numerical code. The SRBS is dominant in the region from the origin below x=100. A result which invites to more investigations in previous results in the study of the amplification of the stimulated Raman backscattering.

Section 4 presents a numerical simulation of the one-dimensional Vlasov-Maxwell equations to study the problem of the amplification of an ultra-short seed pulse via stimulated Brillouin backscattering, by the interaction with a long pulse pump assumed to have an envelope that is constant in amplitude before interaction, the amplification is mediated by an IAW. In the example we present in section 4, we use the parameters which have been used in the simulations using PIC codes in Andreev et al., [27], with a length of $273c/\omega_{pe}$ and in Humphrey, et al., [28], with a length of $1000c/\omega_{pe}$, but we have substantially increased to $1600c/\omega_{pe}$ the plasma amplifier length in section 4 in the present work. In the study we presented in Shoucri et al., we used the Vlasov code for a length of the system of $1000c/\omega_{pe}$ [19]. For such a length of interaction, in the PIC simulation of Humphrey, et. al., a collision term has been added in an attempt to damp the numerical noise, and extend the amplification length to $1000c/\omega_{pe}$, but the pump becomes depleted due to scattering from numerical noise, and the signal completely distorted [28]. The results presented in Shoucri et al., [19], allowed a complete solution of the problem for the length of the system of $1000c/\omega_{pe}$, which compares much more favourably with the solution obtained from the noisy PIC code of Humphrey et al.,[28]. We identified the modes excited and followed with accuracy the growth and evolution of the seed pulse. Detailed study of the calculation of the theoretical spectra and the spectra calculated numerically have been presented, together with the evolution of the phase-space, in Shoucri et al., [19]. In the simulation results we present here in section 4, the noiseless Vlasov code allows to follow the amplification of the seed pulses by Brillouin backscattering until the formation of steep gradient of the amplified pulse makes the grid resolution of the steep gradient cannot be resolved anymore. In the simulation results presented here, the simulation length L_p=$1600c/\omega_{pe}$ is about 6 times the length of $273c/\omega_{pe}$ used in Andreev et al., [27]. The pump is running until it reaches x=1600, when the precursor of the pump reaches the right boundary without any numerical problem, and then the growing seed pulse is running backward from x=1600 down to x= 500 at t=2821, a distance of 1100, see Figure (11). Interesting phase-space contour plots are presented in Figure (15) and (16) for the ions and electrons distribution functions, until at the end of the simulation at time t=2821. More details on the study of the excited modes can be found in Shoucri et al., [19].

There have been important developments in the last few decades on the application of Eulerian codes for the numerical solution of the kinetic equations of plasmas. Of special interest are the Eulerian codes based on the method of characteristics for hyperbolic differential equations, where this approach has become increasingly important, especially for the numerical solution of the hyperbolic type Vlasov-Maxwell equations, which are used to study the transport processes when the collisions in plasmas between the particles are negligible, as in high temperature and low-density plasmas. Also, because of the absence of numerical noise, they allow an accurate study of the phase-space dynamics, especially in the low-density region of the phase-space. We have presented two examples in section 3 and section 4. We mention few

more applications of these methods such as the amplification of seed pulses by Raman and Brillouin backscattering in the presence of an external magnetic field, which are important in connection with the amplification of whistler pulses along the magnetic field of the earth. See also the recent work in [22,23,29].

We mention for reference interesting further applications of the Eulerian Vlasov codes, the problem of ion acceleration and plasma jet formation in the interaction of a high intensity laser beam normally incident on an overdense plasma [30,31,33]. The problem of the wakefield acceleration has been studied in Shoucri [32]. The Eulerian Vlasov code has been previously successfully applied to study stimulated Raman scattering of plane waves in an underdense plasma [21,24,25,34-37]. See also Strozzi et al.,[38] Arber et al., [39]. A study on the formation of electric field at the edge of a plasma, especially important in the physics of Tokamaks, has been presented in Shoucri et al., [5,6,40,41]. A study of the plasma sheath at a plasma-wall transition has been presented in Shoucri et al., [42]. For more information on the applications of cubic splines and numerical methods to problems involving Eulerian Vlasov codes, see Pohn [43].

Acknowledgements: The author acknowledges fruitful discussions with Dr. B Afeyan on kinetic electrostatic electron nonlinear (Keen) waves, and fruitful discussions with Dr. F.Vidal and Dr. J. P. Matte

References

1. Shoucri M (2010a) Editor: Eulerian Codes for the Numerical Solution of the Kinetic Equations of Plasmas. Nova Science Publishers: New York, USA.
2. Shoucri M (2008a) The Application of the Method of Characteristics for the Numerical Solution of Hyperbolic Differential Equations. Nova Science Publishers: New York, USA.
3. Shoucri M (2008b) Numerical Solution of Hyperbolic Differential Equation. Nova Science Publishers New York, USA.
4. Shoucri M (2009) Advances in Mathematic Research. Baswell AR Ed 8: 1-87.
5. Shoucri M, Gerhauser H, Finken KH (2003) Integration of the Vlasov Equation along Characteristics in One and Two Dimensions. Comp Phys Comm 154: 65-75.
6. Shoucri M, Gerhauser H, Finken KH (2004) Study of the Generation of a Charge Separation and Electric Fields at a Plasma Edge using Eulerian Vlasov Codes in Cylindrical Geometry. Comp Phys Comm 164: 168-179.
7. Drake JF, Kaw PK, Lee YC, Schmidt G, Liu CS, et al. (1974) Parametric instabilities of electromagnetic waves in plasmas. Phys Fluids 17: 778-785.
8. Malkin VM, Toroker Z, Fisch NJ (2014) Saturation of the leading spike growth in backward Raman amplifiers. Phys Plasmas 21: 093112.
9. Max CE, Arons J, Langdon AB (1974) Self-Modulation and Self-Focusing of Electromagnetic Waves in Plasmas. Phys Rev Lett 33: 209-212.
10. Kruer W (1988) The Physics of Laser-Plasma Interaction. Available at: https://www.cambridge.org/core/journals/journal-of-plasma-physics/article/abs/physics-of-laser-plasma-interactions-w-l-kruer-addisonwesley-1988-3395-182-pages/A9B7C4049389ED242AFA88E608AAC7EF.
11. Mourou GA, Fisch N, Malkin V, Toroker Z, Khazanov E, et al. (2012) Exawatt-Zettawatt pulse generation and applications. Opt Common 285: 720-724.
12. Riconda C, Weber S, Lancia L, Marquès JR, Mourou GA, et al. (2013) Spectral characteristics of ultra-short laser pulses in plasma amplifiers. Phys Plasmas 20: 083115.
13. Benisti D, Yampolsky NA, Fisch NJ (2012) Comparisons between nonlinear kinetic modelings of simulated Raman scattering using envelope equations. Phys Plasmas 19: 013110.
14. Lehmann G, Spatschek K-H (2013) Nonlinear Brillouin Amplification of Finite-Duration Seeds in the Strong Coupling Regime. Phys Plasmas 20: 073112.
15. Lehmann G, Spatschek KH (2014) Reflection and transmission properties of a finite-length electron plasma grating. Matter and Radiation at Extremes 7: 054402.
16. Wang TL, Clark DS, Strozzi DJ, Wilks SC, Martins SF, et al. (2010) Particle-in-cell simulations of kinetic effects in plasma-based backward Raman amplification in underdense plasmas. Phys Plasmas 17: 023109.
17. Toroker Z, Malkin VM, Fisch NJ (2014) Backward Raman amplification in the Langmuir wavebreaking regime. Phys Plasmas 21: 113110.
18. Shoucri M, Afeyan B (2014) Numerical Simulation of Raman Scattering with a Relativistic Vlasov-Maxwell code: a cascade of nonstationary nonlinear interactions. In Computational and Numerical Simulations. Available at: https://www.intechopen.com/chapters/46146.
19. Shoucri M, Matte JP, Vidal F (2015) Relativistic Eulerian Vlasov Simulation of the Amplification of Seed Pulses by Brillouin Backscattering in Plasmas. Phys Plasmas 22: 053101.
20. Shoucri M, Afeyan B (2016a) Vlasov-Maxwell simulation of backward Raman Amplification of Seed Pulses in Plasmas. Laser Part Beams 34: 576-600.
21. Califano F, Mangeney A (2010) A Vlasov Approach to Collisionless Space and Laboratory Plasmas. In: Eulerian codes for the numerical solution of the kinetic equations of plasmas. Available at: https://arpi.unipi.it/handle/11568/142772.
22. Califano F, Lontano M (2003) Vlasov-Maxwell Simulations of High-Frequency Longitudinal Waves in a Magnetized Plasma. Phys Rev E 67: 056401.
23. Shoucri M (2016b) Numerical Simulation of Raman and Brillouin Laser-Pulse Amplification in a Magnetized Plasma. Laser Part Beams 34: 315-337.
24. Mangeney A, Califano F, Cavazzoni C, Travnicek PA (2002) Numerical Scheme for the Integration of the Vlasov-Maxwell System of Equations. Jour Comp Phys 179: 495.
25. Ruhl H, Mulser P (1995) Relativistic Vlasov Simulation of Intense Fs Laser Pulse-Matter Interaction. Physics Letters A 205: 388-392.
26. Bers A, Shkarofsky I, Shoucri M (2009) Relativistic Landau Damping of Electron Plasma Waves in Stimulated Raman Scattering. Phys Plasmas 16: 022104.
27. Andreev A, Riconda C, Tichonchuk V, Weber S (2006) A Vlasov code simulation of the amplification of seed pulses by Brillouin backscattering in plasmas. Phys Plasmas 13: 053110.
28. Humphrey KA, Trines RMGM, Fiuza F, Speirs DC, Norreys P, et al. (2013) Effect of collisions on amplification of laser beams by Brillouin scattering in plasmas. Phys Plasmas 20: 102114.
29. Shoucri M (2025) Ion Acceleration and Plasma Jet Formation: Amplification of a Whistler Pulse along a Magnetic Field,

Interaction of a Relativistic Electron Beam with a Plasma, Eulerian Vlasov Codes for Laboratory and Space Plasma Simulation. Jour High Energy Phys Gravitation Cosmology 11: 1566-1594.

30. Shoucri M (2010b) Numerical solution of the relativistic Vlasov-Maxwell equations for the study of the interaction of a high intensity laser beam normally incident on an overdense plasma. Eulerian codes for the numerical solution of the kinetic equations of plasmas pp: 163-236.
31. Shoucri M (2012a) Ion acceleration and plasma jet formation in the interaction of an intense laser beam normally incident on an overdense plasma: a Vlasov code simulation. Comput Sci Discov 5: 014005.
32. Shoucri M (2008c) Numerical Simulation of Wake-field Acceleration using an Eulerian Vlasov code. Comm Com Phys 4: 703.
33. Shoucri M, Vidal F, Matte JP (2016b) A Numerical Study of Ponderomotive Ion Acceleration in a Dense Plasma driven by a Circularly Polarized High-Intensity Laser Beam Normally Incident on Thin Foils. Laser Part Beams 34: 242-262.
34. Bertrand P, Ghizzo A, Johnston TW, Shoucri M, Fijalkow E, et al. (1990) A Non-Periodic Euler-Vlasov Code for the Numerical Simulation of Laser-Plasma Acceleration and Plasma Scattering. Phys Fluids B 2: 1028.
35. Ghizzo A, Bertrand P, Shoucri M, Johnston TW, Fijalkow E, et al. (1990) A Vlasov Code for the Numerical Simulation of Stimulated Raman Scattering. Jour Comp Phys 90: 431-457.
36. Shoucri M (2008d) Eulerian Codes for the Numerical Solution of the Vlasov Equation. Comm Nonl Sci Num Simul 13: 174-182.
37. Bertrand P, Ghizzo A, Karttunen S, Pattikangas T, Salomaa R, et al. (1992) Simulations of Wave-Particle Interactions in Stimulated Raman Forward Scattering in a Magnetized Plasma. Phys Fluids B 4: 3950.
38. Strozzi DJ, Langdon AB, Williams EA, Bers A, Brunner S (2010) Eulerian-Lagrangian Kinetic Simulations of Laser-Plasma Interactions. Available at: https://www.davidstrozzi.info/Vlasbook-srs-djs.pdf.
39. Arber TD, Sircombe NJ, Vann RGL (2010) Eulerian Conservative Advection Schemes for Vlasov Solvers. Available at: https://pure.york.ac.uk/portal/en/publications/eulerian-conservative-advection-schemes-for-vlasov-solvers/.
40. Shoucri M (2018) Comments on Equilibrium Potential Well due to Finite Larmor Radius Effect on the Tokamak Edge. Phys Plasmas 25: 054701.
41. Shoucri M (2012b) Charge Separation and Electric Field at a Cylindrical Plasma Edge. Numerical Simulation: From Theory to Industry. Available at: https://www.intechopen.com/chapters/39217.
42. Shoucri M, Gerhauser, H, Finken K-H (2009) Oscillations of the Collisionless Sheath at Grazing Incidence of the Magnetic Field. Phys Plasmas 16: 103506.
43. Pohn E (2001) Numerishe Simulation des Anomalen Transportes in der Plasmarandschicht. Ph.D. Dissertation. Technische Universität Wien Austria. Available at: https://repositum.tuwien.at/handle/20.500.12708/179021.